

CDK5–cyclin B1 regulates mitotic fidelity

<https://doi.org/10.1038/s41586-024-07888-x>

Received: 24 March 2023

Accepted: 30 July 2024

Published online: 4 September 2024



Xiao-Feng Zheng^{1,8}, Aniruddha Sarkar^{1,8}, Humphrey Lotana², Aleem Syed¹, Huy Nguyen¹, Richard G. Ivey³, Jacob J. Kennedy³, Jeffrey R. Whiteaker³, Bartłomiej Tomasiłk^{1,4,7}, Kaimeng Huang^{1,5}, Feng Li¹, Alan D. D'Andrea^{1,5}, Amanda G. Paulovich³, Kavita Shah², Alexander Spektor^{1,5,✉} & Dipanjan Chowdhury^{1,5,6,✉}

CDK1 has been known to be the sole cyclin-dependent kinase (CDK) partner of cyclin B1 to drive mitotic progression¹. Here we demonstrate that CDK5 is active during mitosis and is necessary for maintaining mitotic fidelity. CDK5 is an atypical CDK owing to its high expression in post-mitotic neurons and activation by non-cyclin proteins p35 and p39². Here, using independent chemical genetic approaches, we specifically abrogated CDK5 activity during mitosis, and observed mitotic defects, nuclear atypia and substantial alterations in the mitotic phosphoproteome. Notably, cyclin B1 is a mitotic co-factor of CDK5. Computational modelling, comparison with experimentally derived structures of CDK–cyclin complexes and validation with mutational analysis indicate that CDK5–cyclin B1 can form a functional complex. Disruption of the CDK5–cyclin B1 complex phenocopies CDK5 abrogation in mitosis. Together, our results demonstrate that cyclin B1 partners with both CDK5 and CDK1, and CDK5–cyclin B1 functions as a canonical CDK–cyclin complex to ensure mitotic fidelity.

Cell division is regulated by cyclin-dependent kinases (CDKs), a family of serine/threonine kinases, and their binding partners cyclins. Approximately 20 CDKs and 29 cyclins have been identified in higher eukaryotes largely based on homology. However, only a limited number of CDK–cyclin complexes have been functionally characterized as cell cycle regulators³. Progression through DNA replication, or S phase, is regulated by CDK2 in a complex with cyclin E and subsequently with cyclin A⁴. Cyclin B1 binds to CDK1 with high affinity^{5–7} and forms the primary CDK complex necessary for progression and completion of mitosis^{1,8,9}. Cyclin B1 first appears in S phase, then accumulates during G2 and mitosis, and finally is degraded rapidly at the onset of anaphase^{10,11}. Timely mitotic exit is dependent on optimal cyclin B1 levels and CDK1 activity^{11,12}. While recent studies have shown a considerable overlap in substrate specificities between M-phase and S-phase CDKs in yeast¹³, CDK2 is unable to compensate for the loss of CDK1 in mammalian cells in completing mitosis¹⁴. The question is whether other CDKs are necessary for mitotic fidelity.

In our previous study, we observed that CDK5 is active throughout mitosis¹⁵. Despite sharing 60% sequence homology with the known cell-cycle-relevant CDKs CDK1 and CDK2, CDK5 has not been found to be activated by cyclins or to directly regulate the cell cycle in proliferating cells². CDK5 was therefore classified as an atypical CDK. CDK5 has the highest expression and is most active in post-mitotic neurons¹⁶. Concordantly, the activating co-factors for CDK5, p35 and p39, and their calpain-cleaved stabilized forms, p25 and p29, respectively, are non-cyclin proteins expressed in cells of neuronal origin^{2,17}. The CDK5–p35 complex is essential for regulating the cytoskeletal architecture of neurons that facilitates dendrite formation, axon guidance and neuronal migration necessary for the development of the central nervous system². Recent studies have identified extraneuronal functions of

CDK5 in apoptosis, metabolism, immune function, angiogenesis, myogenesis, cell migration and invasion¹⁸. Furthermore, overexpression or hyperactivation of CDK5 has been associated with poor prognosis across many cancer types¹⁷. The study of the role of CDK5 in cell cycle events faces challenges stemming from the lack of specificity in CDK5 inhibitors, non-physiological compensation due to prolonged CDK5 depletion by CRISPR–Cas9, and potential off-target and acute effects of short interfering RNA treatments. To overcome these limitations and test the role of CDK5 in mitosis, here we used two independent strategies to specifically abrogate CDK5 activity in mitosis at a high temporal resolution.

CDK5 is required for mitotic fidelity

To delineate the mitotic functions of CDK5, we generated two independent chemical genetic systems to inactivate CDK5 in a specific and temporally regulated manner. First an analogue-sensitive variant of CDK5 containing a F80G mutation (hereafter, CDK5(as)) was expressed in RPE-1 cells^{19,20}. This substitution creates an enlarged ATP-binding pocket that is absent in wild-type CDK5 but does not alter CDK5 catalysis or specificity. Introduction of bulky orthogonal inhibitors such as 1NM-PP1 or 3MB-PP1 that occupy the enlarged ATP-binding pocket selectively inhibits the CDK5(as) variant but does not inhibit wild-type CDK5^{15,19,20} (Extended Data Fig. 1a). We subsequently knocked out endogenous CDK5 using CRISPR–Cas9 such that only the CDK5(as) variant remains expressed (Extended Data Fig. 1b). We next compared the growth rate of RPE-1 CDK5(as) cells with that of parental RPE-1 cells to confirm that expression of Flag–HA–CDK5(as) does not affect cell proliferation (Extended Data Fig. 1c). We also ascertained that the orthogonal inhibitor 1NM-PP1 specifically inhibited CDK5(as) but not CDK1 in mitosis

¹Division of Radiation and Genome Stability, Department of Radiation Oncology, Dana-Farber Cancer Institute, Harvard Medical School, Boston, MA, USA. ²Department of Chemistry and Purdue University Center for Cancer Research, Purdue University, West Lafayette, IN, USA. ³Translational Science and Therapeutics Division, Fred Hutchinson Cancer Research Center, Seattle, WA, USA. ⁴Department of Biostatistics and Translational Medicine, Medical University of Lódz, Lódz, Poland. ⁵Broad Institute of Harvard and MIT, Cambridge, MA, USA. ⁶Department of Biological Chemistry & Molecular Pharmacology, Harvard Medical School, Boston, MA, USA. ⁷Present address: Department of Oncology and Radiotherapy, Medical University of Gdańsk, Faculty of Medicine, Gdańsk, Poland. ⁸These authors contributed equally: Xiao-Feng Zheng, Aniruddha Sarkar. [✉]e-mail: Alexander_Spektor@dfci.harvard.edu; Dipanjan_Chowdhury@dfci.harvard.edu

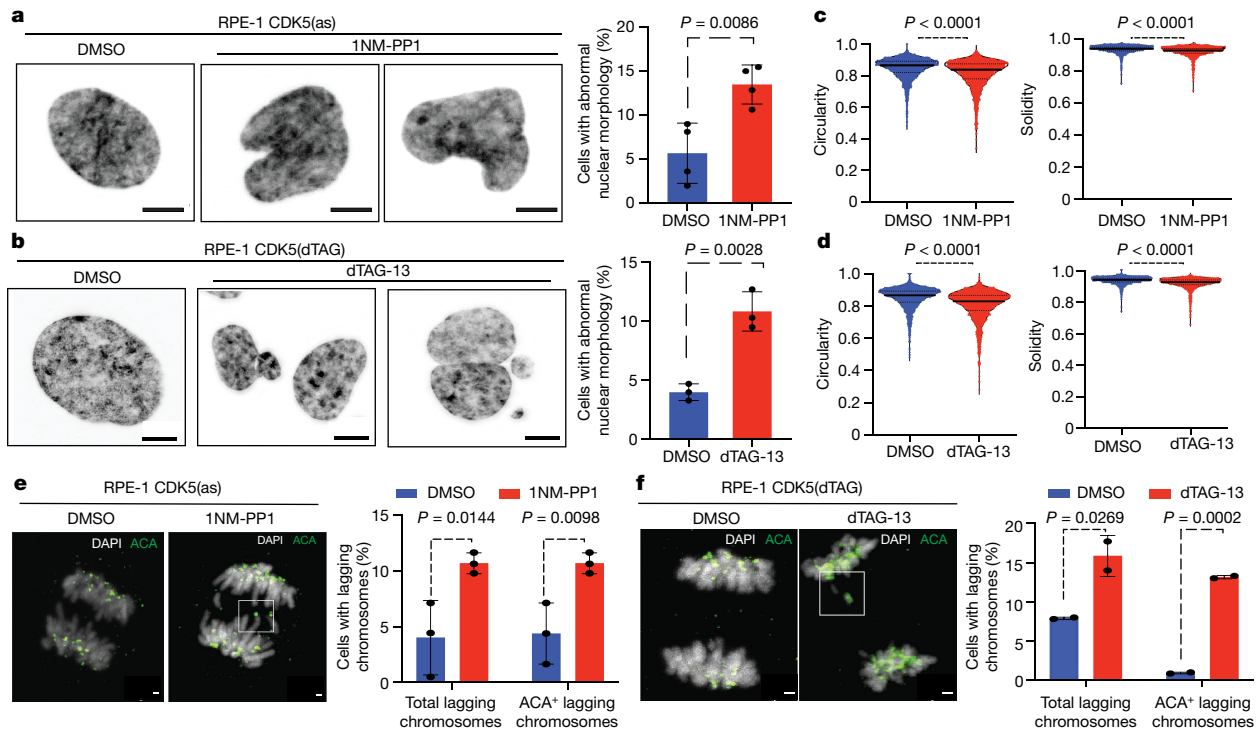


Fig. 1 | Abrogation of CDK5 leads to abnormal nuclear morphology, lagging chromosomes and micronuclei. **a,b**, Hoechst staining showing the nuclear morphology of RPE-1 CDK5(as) (**a**) and RPE-1 CDK5(dTAG) (**b**) cells with the indicated treatment, fixed at 120 min after release from RO-3306-induced arrest at G2/M (left). Right, the percentage of cells displaying abnormal nuclear morphology after the indicated treatment. **c,d**, Quantification of nuclear circularity and solidity of RPE-1 CDK5(as) (**c**) and CDK5(dTAG) (**d**) cells from the experiment shown in **a** and **b**, respectively. **e,f**, Representative images of RPE-1 CDK5(as) (**e**) and CDK5(dTAG) (**f**) cells exhibiting ACA-positive lagging

chromosomes after the indicated treatments (left). Lagging chromosomes are indicated by the punctate squares. Right, quantification of the percentage of cells exhibiting total lagging chromosomes and ACA-positive lagging chromosomes after the indicated treatments. For **a–f**, data are mean \pm s.d. of three (**a–e**) or at least two (**f**) independent experiments from $n = 2,174$ (DMSO) and $n = 1,788$ (1NM-PP1) (**a** and **c**); $n = 2,094$ (DMSO) and $n = 2,095$ (dTAG-13) (**b** and **d**); and $n = 300$ (each condition; **e** and **f**) anaphase cells. P values were calculated using unpaired two-tailed Student's *t*-tests. Scale bars, 1 μ m (**e** and **f**) and 5 μ m (**a** and **b**).

by measuring the kinase activity of endogenous CDK1 and CDK5(as) immunoprecipitated from mitotic RPE-1 CDK5(as) cells treated with DMSO or 1NM-PP1. CDK5(as), but not CDK1, exhibited diminished kinase activity after treatment with 1NM-PP1 (Extended Data Fig. 1d,e). Treatment with 1NM-PP1 diminished the phosphorylation of PP4R3 β at Ser840, a validated mitotic substrate of CDK5¹⁵, while the levels of PP4R3 β remained unchanged (Extended Data Fig. 1f).

Orthogonally, we used a proteolysis-targeting chimera (PROTAC)-based targeted protein degradation approach. Specifically, we expressed a CDK5 variant fused to the FKBP12(F36V) domain, or the degradation tag (dTAG; hereafter CDK5(dTAG)), in RPE-1 cells. The F36V mutation in the FKBP domain allows the binding of dTAG-13, the PROTAC linker molecule that links the tagged CDK5 to the cereblon-based proteasomal degradation machinery²¹ to acutely degrade CDK5 (Extended Data Fig. 2a). We subsequently knocked out the endogenous CDK5 by CRISPR–Cas9 such that only the CDK5(dTAG) variant is expressed (Extended Data Fig. 2b). We confirmed that RPE-1 CDK5(dTAG)-expressing cells proliferate at a comparable rate to that of parental RPE-1 cells (Extended Data Fig. 2c). Expectedly, introduction of dTAG-13 resulted in specific but heterogeneous degradation of CDK5, as PROTAC strategies rely on endogenous cellular machinery to mediate degradation of the protein of interest, of which the subcellular location and access to the E3 ligase can impact PROTAC efficiency²² (Extended Data Fig. 2d,e). Importantly, degradation of CDK5 consequently led to the diminished phosphorylation of PP4R3 β at Ser840, while levels of PP4R3 β , related cyclin-dependent kinases CDK1 and CDK2, and CDK1 co-factor cyclin B1 remained unchanged (Extended Data Fig. 2f).

With the CDK5-specific abrogation systems and the kinetics of CDK5 abrogation established before and on entry into mitosis, we arrested

CDK5(as)- or CDK5(dTAG)-expressing RPE-1 cells at the G2/M border by treatment with the CDK1 inhibitor RO-3306²³. 1NM-PP1 or dTAG-13 was introduced to CDK5(as) and CDK5(dTAG) cells, respectively, 2 h before release from RO-3306 to initiate CDK5 inhibition or degradation such that a majority of CDK5 would be abrogated before mitotic entry. Medium containing 1NM-PP1 or dTAG-13 was added to cells after release from RO-3306 to ensure continued CDK5 abrogation throughout mitosis (Extended Data Figs. 1g and 2g).

To assess the role of CDK5 during mitosis, we first determined whether catalytic inhibition or degradation of CDK5 after one round of mitosis leads to mitotic abnormalities. Catalytic inhibition of CDK5(as) by 1NM-PP1 and degradation of CDK5(dTAG) by dTAG-13 resulted in the development of abnormal nuclear morphologies with extensive nuclear lobulation after exit from the initial mitosis (Fig. 1a,b). Quantitative analysis of established nuclear shape parameters, circularity and solidity²⁴, confirmed the presence of abnormal nuclear morphologies after inhibition of CDK5(as) by 1NM-PP1 and degradation of CDK5(dTAG) by dTAG-13, as evidenced by the decrease in circularity and solidity after exit from the initial mitosis (Fig. 1c,d). As nuclear abnormalities are suggestive of chromosome mis-segregation, we quantified cells with lagging chromosomes in response to CDK5 abrogation. Abrogation of CDK5 in CDK5(as) and CDK5(dTAG) cells resulted in an increase in lagging chromosomes that stained positively with anticentromere antibody (ACA), indicating a whole-chromosome mis-segregation defect rather than generation of acentric fragments (Fig. 1e,f). Concordantly with the increase in lagging chromosomes, we observed an increase in micronuclei in cells abrogated of CDK5 by 1NM-PP1-induced inhibition or dTAG-13-induced degradation (Extended Data Figs. 1h and 2h).

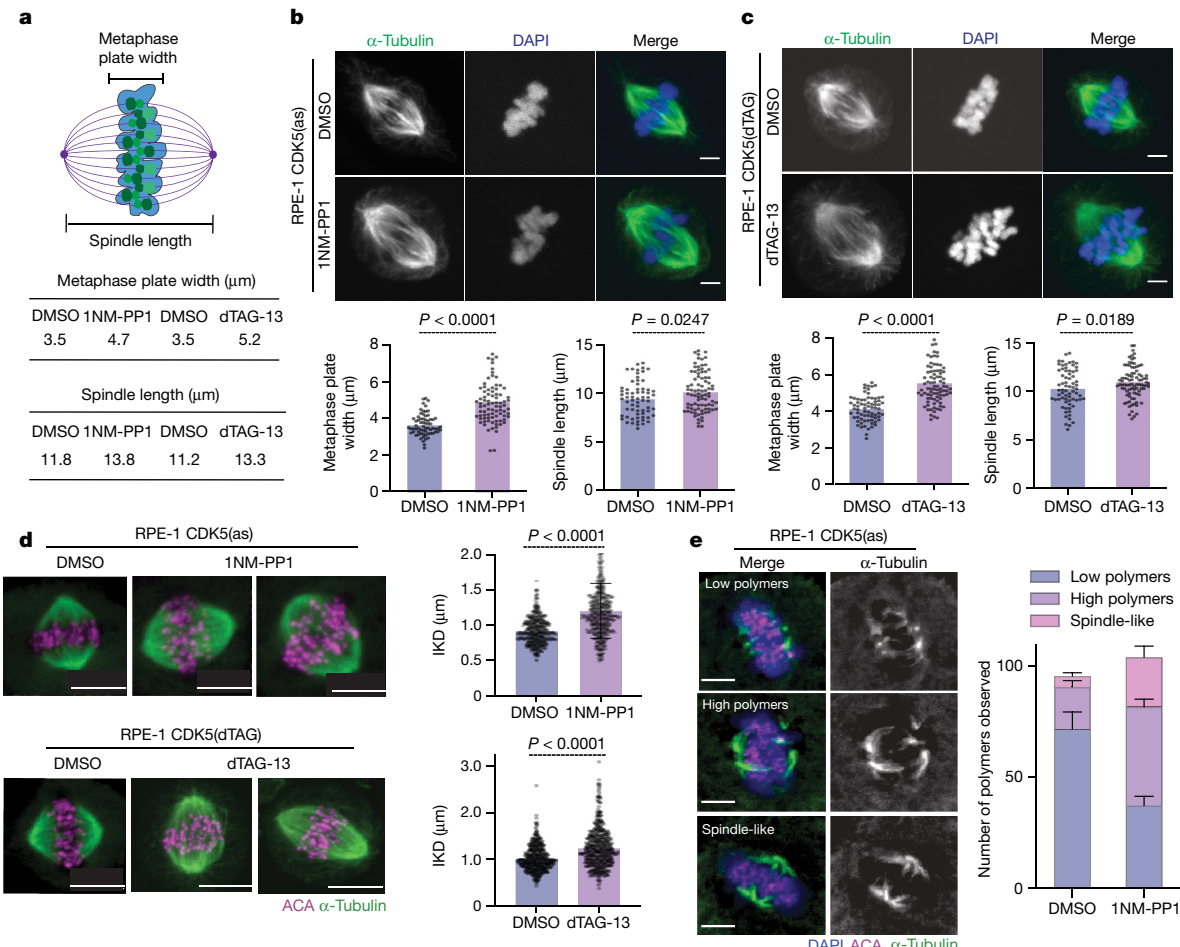


Fig. 2 | Abrogation of CDK5 leads to chromosome alignment defects and abnormal spindle architecture. **a**, Schematic of the spindle structure parameters measured in **b** and **c**. **b,c**, Representative images of RPE-1 CDK5(as) (**b**) and RPE-1 CDK5(dTAG) (**c**) cells treated as indicated, released from RO-3306 into medium containing 20 μM proTAME for 2 h and stained for α -tubulin and with DAPI (top). Metaphase plate width and spindle length measurements for these representative cells are shown in the table on the left. Quantification of the metaphase plate width and spindle length after the indicated treatments (bottom). **d**, Representative images of RPE-1 CDK5(as) and/or RPE-1 CDK5(dTAG) cells that were treated as indicated, released from RO-3306 into medium containing 20 μM proTAME for 2 h and stained for α -tubulin (green) and with ACA (magenta) (left). Quantification of IKD as measured by the distance

between two sister kinetochores stained with ACA after the indicated treatments as described (right). **e**, Representative images of metaphase RPE-1 CDK5(as) cells, showing the indicated spindle microtubule polymer levels, as described previously²⁹, after the cells were exposed to cold-shock treatment (left). Right, quantification of the frequency of the indicated spindle microtubule polymer levels observed after cold-shock treatment. For **b–e**, data are mean \pm s.d. of three independent experiments from $n = 121$ (DMSO), $n = 182$ (1NM-PP1) (**b**), $n = 134$ (DMSO), $n = 176$ (dTAG-13) (**c**) metaphase cells; $n = 498$ (DMSO; top), $n = 497$ (1NM-PP1), $n = 522$ (DMSO; bottom) and $n = 562$ (dTAG-13) (**d**) kinetochores; and $n = 50$ (each condition) (**e**) metaphase cells. P values were calculated using unpaired two-tailed Student's *t*-tests. Scale bars, 5 μm (**b–e**).

These results suggest that CDK5 abrogation in mitosis leads to whole-chromosome mis-segregation.

CDK5 loss leads to hyperstable spindles

We next investigated the cause of whole-chromosome mis-segregation after CDK5 loss. Lagging chromosomes could arise from kinetochore-microtubule attachment defects²⁵ and/or impaired correction of erroneous kinetochore-microtubule attachments^{26,27}. We first determined whether chromosomes in cells abrogated for CDK5 can align properly at metaphase plate. We monitored RPE-1 CDK5(as) and CDK5(dTAG) cells expressing fluorescent histone (mCherry-H2B) and microtubule (GFP- α -tubulin) markers after CDK5 abrogation using high-resolution live-cell imaging from prophase until the end of mitosis (Extended Data Fig. 3a,b and Supplementary Videos 1–6). In contrast to DMSO-treated cells, CDK5(as) and CDK5(dTAG) cells that were treated with 1NM-PP1 and dTAG-13, respectively, resulted in the formation of abnormal nuclear morphologies after mitotic exit (Extended Data Fig. 3a,b) owing

to a higher frequency of chromosome alignment defects in metaphase (Extended Data Fig. 3c,d). To ascertain the chromosome alignment defect, we synchronized CDK5(as) and CDK5(dTAG) cells, abrogated for CDK5, in late metaphase by treatment with the APC/C inhibitor proTAME²⁸, which blocks progression into anaphase, and observed a significant increase in metaphase plate width and mitotic spindle length in both CDK5(as) and CDK5(dTAG) cells abrogated for CDK5 compared with the DMSO controls (Fig. 2a–c). These results further corroborate our observation from high-resolution live-cell imaging experiments that the loss of CDK5 leads to chromosome alignment errors. The observed increase in spindle length after CDK5 abrogation suggests the potential presence of hyperstable spindle microtubules. This phenomenon is a known contributor to impaired kinetochore-microtubule error correction²⁹ that could be responsible for the observed mitotic defects, including chromosome mis-segregations and nuclear atypia. To assess microtubule stability, we performed two assays. First, we determined the interkinetochore distance (IKD) between the two sister chromatids in metaphase. Hyperstability of spindle microtubules leads

to increased pulling forces, which in turn increases the IKD. Indeed, both CDK5(as) and CDK5(dTAG) cells abrogated for CDK5 showed an increased IKD relative to the DMSO controls (Fig. 2d), supporting our hypothesis that the loss of CDK5 leads to hyperstable MT. Second, we performed a microtubule depolymerization assay²⁹, which enables one to assess spindle the microtubule stability on the basis of the degree of depolymerization that occurs after rapid cold-shock treatment. Indeed, while spindles were largely depolymerized in DMSO-treated CDK5(as) cells with only low polymers remaining in most cases, treatment with 1NM-PP1 resulted in significantly improved preservation of spindle architecture after the cold treatment (Fig. 2e and Extended Data Fig. 3e). Together, these experiments clearly demonstrate that the loss of CDK5 results in hyperstable spindle microtubules, which are unable to efficiently correct erroneous kinetochore–microtubule attachments, leading to chromosome mis-segregation and nuclear atypia (micronuclei and abnormal primary nuclear morphology). We did not observe an increase in the time from nuclear envelope breakdown to anaphase onset in CDK5(as) cells treated with 1NM-PP1 (Extended Data Fig. 3f), indicating that the spindle-assembly checkpoint is not activated after CDK5 abrogation. We further confirmed that the spindle-assembly checkpoint is intact in these cells, as evident by efficient prometaphase arrest after nocodazole treatment (Extended Data Fig. 3g). These observations are consistent with previous studies showing that stabilized, uncorrected merotelic kinetochore–microtubule attachment can lead to chromosome mis-segregation and aneuploidy without triggering spindle-assembly-checkpoint activation^{30–32}. Our results suggest that the observed mitotic errors, including chromosome mis-segregation leading to micronucleation, arise as a consequence of impaired error correction of erroneous kinetochore–microtubule attachment due to hyperstable microtubules.

CDK5 regulates microtubule dynamics

Proper mitotic spindle dynamics that ensure faithful chromosomal segregation depend on the regulation of microtubule building components, α - β -tubulin dimers³³. The CDK1–cyclin B1 complex upregulates microtubule dynamics by phosphorylating tubulins and microtubule effectors^{34,35}. As abrogation of CDK5 hyperstabilizes microtubules, it is conceivable that CDK5, similar to CDK1, may localize to tubulin and regulate microtubule dynamics. Consistent with this hypothesis, CDK5 displayed a similar co-localization pattern to CDK1 throughout mitosis, with the most significant enrichment on spindle microtubules in prometaphase (Extended Data Fig. 4a–d). On the basis of these results, we hypothesize that, like CDK1, CDK5 may phosphorylate factors that regulate microtubule dynamics.

To identify the mitotic substrates of CDK5 that may be responsible for the observed mitotic phenotypes, we conducted quantitative phosphoproteomic profiling of mitotically synchronized RPE-1 CDK5(as) cells (Extended Data Fig. 5a,b). We hypothesized that phosphoproteins downregulated after abrogation of CDK5 by 1NM-PP1-induced inhibition represent putative mitotic substrates of CDK5. We identified 255 phosphorylation sites that were downregulated at least twofold in two independent experiments after CDK5 inhibition by 1NM-PP1 compared with the DMSO controls (Fig. 3a and Supplementary Table 1). These downregulated phosphoproteins were enriched for components of microtubule, mitotic spindle and kinetochore (Fig. 3b), supporting our hypothesis that CDK5 regulates microtubules and other mitotic components. Notably, phosphoproteins upregulated after CDK5 loss were enriched for non-microtubule cytoskeletal regulators and RNA-processing proteins, but not for proteins with a mitotic function (Extended Data Fig. 5c).

The significantly downregulated phosphorylation sites corresponded to established microtubule-interacting proteins and proteins with a known mitotic function, including NUMA1, KIF20A, CKAP2L, CEP170 and NUSAP1 (Extended Data Fig. 5d). Nuclear mitotic apparatus

protein 1 (NUMA1) is a spindle-microtubule-associated protein that localizes to mitotic spindle poles and cortex to organize mitotic spindles and regulates spindle orientation^{36,37}. Phosphorylation of NUMA1 by CDK1 at its C-terminal domain during mitosis regulates its timely localization to cortex in anaphase³⁸. Kinesin family member 20A (KIF20A; also known as MKLP2) is a kinesin motor protein of which phosphorylation at the C terminus, including Ser878 by CDK1–cyclin B1, is required for relocation of chromosome passenger complex to the central spindle after anaphase transition³⁹. In addition to its well-established role in the later stages of mitosis, KIF20A has been implicated in regulating proper chromosome congression⁴⁰. We verified that inhibition of CDK5 by 1NM-PP1 treatment diminished phosphorylation of serine in NUMA1, KIF20A and PP4R3B at the serine–proline CDK substrate motif (Fig. 3c). Furthermore, inhibition of CDK5 resulted in excess accumulation of NUMA1 at the spindle pole (Fig. 3d). As the concentration of NUMA1 at the spindle pole has been shown to regulate mitotic spindle length⁴¹, these results suggest that loss of CDK5-mediated phosphorylation of NUMA1 may contribute to the observed hyperstability of spindle microtubules. NUMA1, KIF20A, NUSAP1, CEP170 and CKAP2L phosphorylation sites identified by CDK5 phosphoproteomics analysis are also predicted to be targeted by CDK1 (Extended Data Fig. 5e), suggesting a functional redundancy between the two CDKs. Together, our phosphoproteomics studies have identified several CDK5 substrates that function in the regulation of microtubule stability during mitosis and may contribute to the observed mitotic phenotype.

Cyclin B1 binds to and activates CDK5

Having established that CDK5 is required for mitotic fidelity, we sought to identify the activator of CDK5 in mitosis. Notably, known activators of CDK5 from neuronal cells and neuroendocrine cells, p35 (also known as CDK5RI) and p39 (also known as CDK5R2), are minimally expressed in mitotic RPE-1 cells and do not interact with CDK5 in mitotic RPE-1 cells (Extended Data Fig. 6a). Thus, in mitotic non-neuronal cells, CDK5 may be activated by an alternative activator. Cyclin B1 localizes to the kinetochore during prometaphase and contributes to kinetochore–microtubule attachment and efficient alignment of chromosomes⁴². These results suggest that cyclin B1 could be a mitotic activator of CDK5 that regulates chromosome alignment. Immunoprecipitation of CDK5 from mitotic RPE-1 cells pulled down cyclin B1 and vice versa (Fig. 4a). We also tested the interaction between cyclin A2, another mitotic cyclin that interacts with and activates CDK1 in early mitosis⁴³, and CDK5. While CDK5 interacts with cyclin A2 in RO-3306-arrested G2 cells, the interaction is much weaker in nocodazole-arrested prometaphase mitotic cells (Extended Data Fig. 6a). Furthermore, in vitro kinase assays showed that cyclin B1 stimulates CDK5 kinase activity, albeit at lower levels than p35 (Fig. 4b). Co-localization analysis of immunofluorescence microscopy images at different stages of mitosis revealed that CDK5 and cyclin B1 displayed similar co-localization patterns to that of CDK1 and cyclin B1, with increasing Manders' coefficients as cells progress from G2 to metaphase (Fig. 4c and Extended Data Fig. 6b). Cyclin-B1-targeted substrates have been catalogued by phosphoproteomics using a strategy of cyclin B1 degradation coupled with distinct cell synchronization methods⁴⁴. Although our methodology for phosphoproteomics analysis differs substantially from that which catalogued cyclin-B1-targeted substrates, there is a notable overlap. Specifically, 42 genes from the putative list of CDK5-targeted substrates identified in our analysis coincide with those revealed in the cyclin-B1-targeted substrate cataloguing (Extended Data Fig. 6c). Together, these results suggest that cyclin B1 forms an active complex with both CDK1 and CDK5 during mitosis.

CDK5–cyclin B1 structure prediction

We used the protein–protein interaction prediction algorithm AlphaFold2-Multimer (AF2) to predict the CDK5–cyclin B1 complex

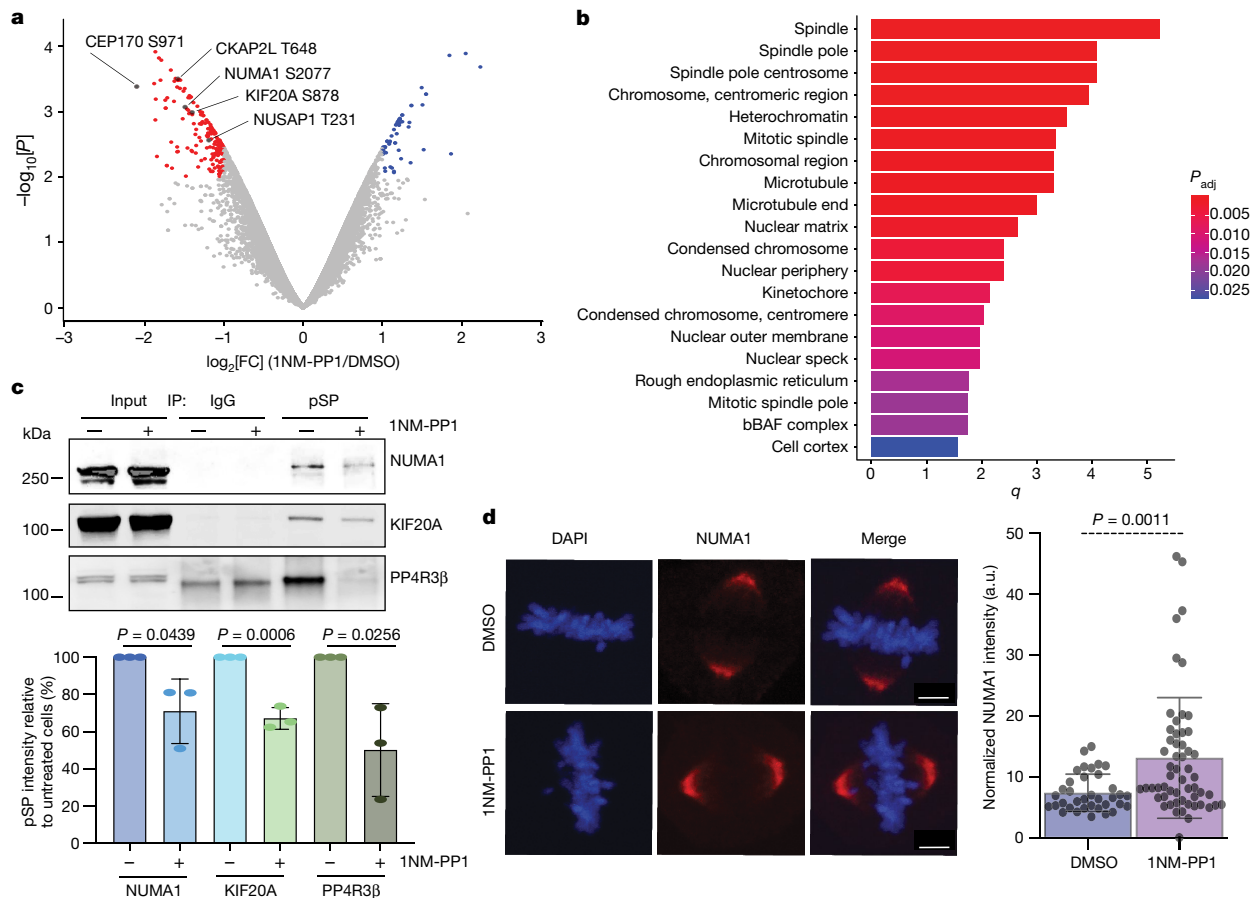


Fig. 3 | Abrogation of CDK5 is associated with reduced phosphorylation of spindle regulators. **a**, Differential phosphosite abundance in 1NM-PP1-treated versus DMSO-treated mitotic RPE-1CDK5(as) cells at 60 min after release from RO-3306-induced synchronization at G2/M. Phosphosites downregulated with a log₂-transformed fold change of lower than -1.0 and $P < 0.01$ as result of 1NM-PP1 treatment are highlighted in red. Phosphosites upregulated with a log₂-transformed fold change higher than 1.0 and $P < 0.01$ as result of 1NM-PP1 treatment are highlighted in blue. Phosphosites downregulated as result of 1NM-PP1 treatment in proteins known to regulate microtubule dynamics are indicated in black. **b**, Gene ontology analysis of downregulated phosphoproteins as a result of CDK5 inhibition. **c**, Immunoblot analysis of phosphorylated Ser/Pro proteins immunoprecipitated from RPE1CDK5(as) cells after the indicated

treatment by anti-phospho-Ser/Pro antibody (pS/P) that recognizes the CDK phosphorylation motif, and immunoblotted with antibodies against the indicated proteins. The pS/P band intensities, quantified by ImageJ, represent the mean \pm s.d. of triplicate repeats of experiments. Uncropped gel images are provided in Supplementary Fig. 1. **d**, Representative images of metaphase RPE-1CDK5(as) cells treated with either DMSO or 1NM-PP1 after release from RO-3306, fixed and stained with antibody against NUMA1 (top). Bottom, quantification of the normalized intensity of NUMA1. For **d**, data are mean \pm s.d. of at least two independent experiments from $n = 35$ (DMSO) and $n = 56$ (1NM-PP1) mitotic cells. For **c** and **d**, P values were calculated using unpaired two-tailed Student's *t*-tests. Scale bars, 5 μ m (**d**).

structure⁴⁵. All of the five output models have interface-predicted template modelling (iPTM) scores of 0.9 or higher and pair-wise structural alignments with a root mean squared deviation of 0.1–0.2 Å (Extended Data Fig. 7a), indicating a high confidence in the predicted CDK5–cyclin B1 models (Extended Data Fig. 7b). The overall conformation of CDK5, especially its PSSALRE helix and the N- and C-terminal lobes in the AF2-predicted model, adopts a canonical cyclin-activated CDK fold⁴⁶. The CDK5 activation loop (amino acids 144–165) in the CDK5–cyclin-B1 complex appears to be in the extended conformation, as seen in fully activated CDK5–p25 and phospho-CDK2–cyclin-A3–substrate structures^{47,48} (Extended Data Fig. 7c).

To further delineate the structural differences between AF2-predicted CDK5–cyclin-B1 complex and experimentally derived CDK5–p25, CKS2–CDK1–cyclin-B1 and phospho-CDK2–cyclin-A3–substrate structures^{6,47,48}, we superimposed these structures (Fig. 4d and Extended Data Fig. 7c). First, we aligned the CDK5–cyclin-B1AF2 structural model to the crystal structure of CDK5–p25 (Fig. 4d). While the overall CDK5 structure in both forms aligns well, there are notable differences in the orientation of the activation loop. The activation loop in the CDK5–p25 complex points upwards in contrast to the downward orientation in the

CDK5–cyclin B1 complex (Fig. 4d). The difference in the activation loop orientation is the result of how the hydrophobic residue (Ile153) at the tip of the CDK5 activation loop is stabilized. In CDK5–p25, Ile153 is stabilized by several surrounding hydrophobic residues (Ala199, Phe203, Met237, Ile275 and Phe282) of p25 from the top. By contrast, Ile153 in the CDK5–cyclin-B1 complex is stabilized by hydrophobic residues (Leu166, Val171 and Ile174) of cyclin B1 from the bottom. The other major difference between these two complexes is that the loop connecting $\alpha 4-\eta 1$ helices in p25 is in a very close proximity to the Ser159 (a putative phosphorylation site for CDK5) in the activation loop in contrast to the similar loop connecting the $\alpha 4-\alpha 5$ helices in cyclin B1 (Fig. 4d and Extended Data Fig. 7d). This proximity precludes the phosphorylation of Ser159 in CDK5 in the CDK5–p25 complex, as the S159E mutant was shown to disrupt the CDK5–p25 interaction⁴⁸. However, this steric hindrance is not present for Ser159 in the CDK5–cyclin B1 complex. Moreover, the orientation of Val163 in the activation loop of CDK5 in CDK5–cyclin B1 aligns perfectly with the Val163 in CDK5–p25 and Val164 in phospho-CDK2–cyclin-A–substrate complex (Extended Data Fig. 7c (left)). This conformation of valine in the activation loop had been shown to be important for the specificity against CDK substrates with

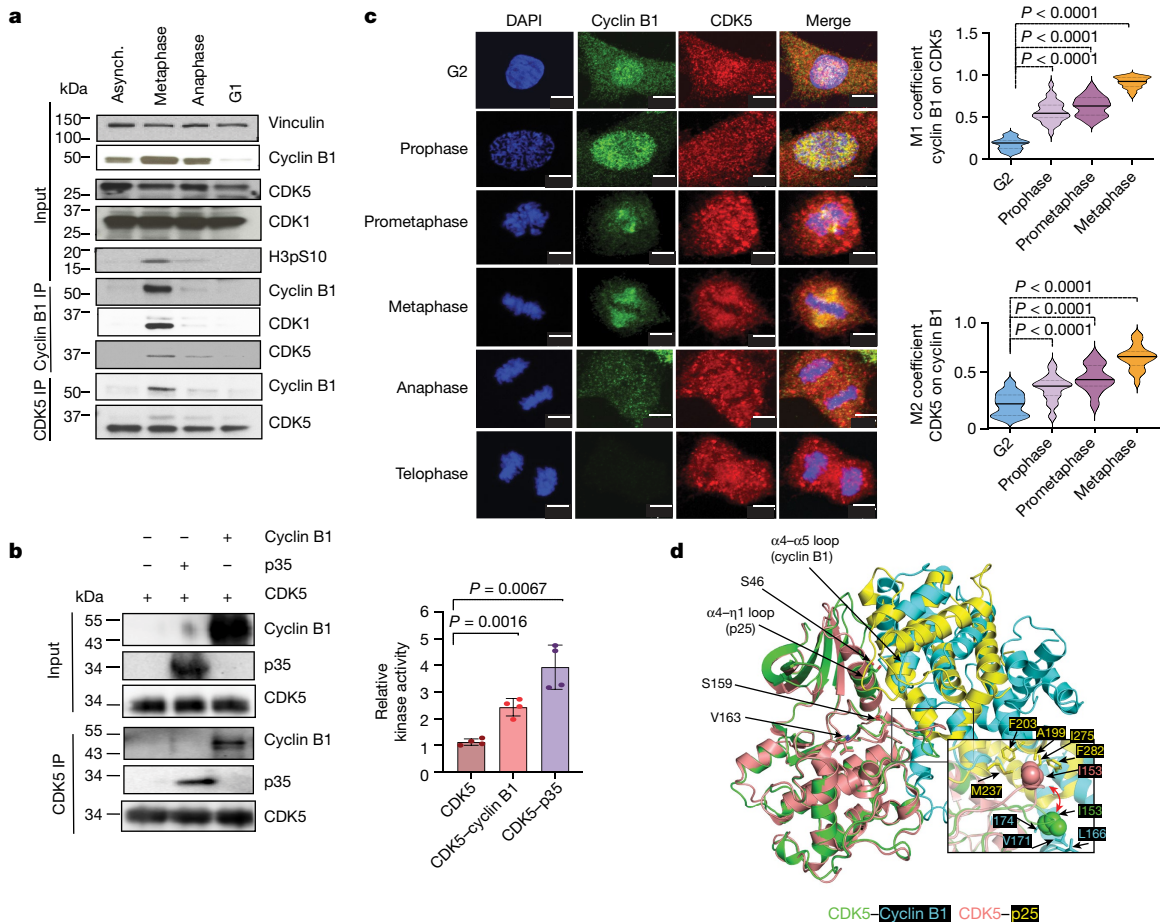


Fig. 4 | Cyclin B1 forms a complex with and activates CDK5 in mitosis. **a**, Endogenous CDK5 or cyclin B1 was immunoprecipitated from HeLa cells, collected at timepoints corresponding to the indicated representative stage in mitosis after release from nocodazole-induced arrest at prometaphase, and immunoblotted using antibodies against the indicated proteins. Asynch., asynchronous. Representative results are shown from two independent repeats. **b**, Immunoblot analysis of CDK5 immunoprecipitation from insect cell lysate overexpressing human CDK5, mixed with bacterial lysate overexpressing the indicated CDK5 co-factors (left). Right, in vitro kinase activity of the immunoprecipitated kinase complex. Data are mean \pm s.d. from

four independent experiments. Uncropped gel images of **a** and **b** are provided in Supplementary Fig. 1. **c**, Immunostaining showing the localization of the indicated proteins in RPE-1 cells at the indicated stages of mitosis (left). Right, the Manders' overlap coefficient M1 (cyclin B1 on CDK5) and M2 (CDK5 on cyclin B1) for cells. Data are mean \pm s.d. of at least two independent experiments from $n = 30$ cells in each stage of mitosis. **d**, Overlay of the CDK5 (green)-cyclin B1 (cyan) model complex on the CDK5 (peach)-p25 (yellow) crystal structure (Protein Data Bank (PDB): 3QOG). Inset: the CDK5 activation loop positioning in both complexes. P values were calculated using unpaired two-tailed Student's t -tests (**b** and **c**). Scale bars, 5 μ m (**c**).

a proline at the +1 position⁴⁸. When we compared the CDK5-cyclin-B1 AF2 model to the crystal structure of CDK1-cyclin-B1-CKS, the activation loop of CDK1 does not appear to align well with CDK5 (Extended Data Fig. 7c (middle)). This could be due to the inherent flexibility of the CDK1 activation loop, which is not resolved completely in the crystal structure and may also be representing a partially activated state of CDK1. However, when we compared to a predicted model of the CDK1-cyclin-B1 complex, we see excellent agreement between the AF2-predicted CDK5-cyclin-B1 and CDK1-cyclin-B1 structures, indicating that the predicted structure of CDK1-cyclin B1 may represent a completely activated form of the complex (Extended Data Fig. 7c (right)). Thus, our computational modelling data indicate that CDK5 and cyclin B1 can form an active protein complex, further supporting in vitro co-localization, co-immunoprecipitation and kinase activity data (Fig. 4a–c).

Phosphorylation at Ser159 activates CDK5

The activation mechanism feature of the CDK5-p25 complex that distinguishes this complex from cell-cycle-relevant CDK1-cyclin and CDK2-cyclin complexes is that the CDK5 active T-loop conformation

is not stabilized by phosphorylation at Ser159, an analogue of Thr161 in the T-loop of CDK1 (Extended Data Fig. 8a,b), but by extensive interaction with the regulator p25^{48,49}. S159A does not abrogate CDK5 kinase activity in neuronal cells due to competent interaction with p25⁴⁸. CDK5 Ser159 is phosphorylated in mitosis (Extended Data Fig. 8c). We therefore determined whether Ser159 phosphorylation is required for interaction with cyclin B1 and subsequent activation of CDK5 in mitosis. CDK5(S159A) retains interaction with cyclin B1 but exhibits diminished CDK5 kinase activity (Extended Data Fig. 8d). To assess the impact of S159A on mitosis, we expressed MYC-His-tagged CDK5(WT) or CDK5(S159A) in RPE-1 CDK5(as) cells and inactivated CDK5(as) with 1NM-PP1 after mitotic entry, leaving the expressed MYC-His-tagged WT or S159A as the only available CDK5 variant present during mitosis (Extended Data Fig. 8e). Compared with CDK5(as) cells expressing WT CDK5, cells expressing empty vector (EV) or the CDK5(S159A) variant displayed abnormal nuclear morphology, as evident from the reduced nuclear circularity and solidity (Extended Data Fig. 8f). Concordantly, cells expressing CDK5(S159A) also displayed abnormal chromosome alignment (Extended Data Fig. 8g and Supplementary Videos 7–10). Cells expressing CDK5(S159A) also phenocopied cells abrogated for CDK5 in terms of increased metaphase plate width and spindle length

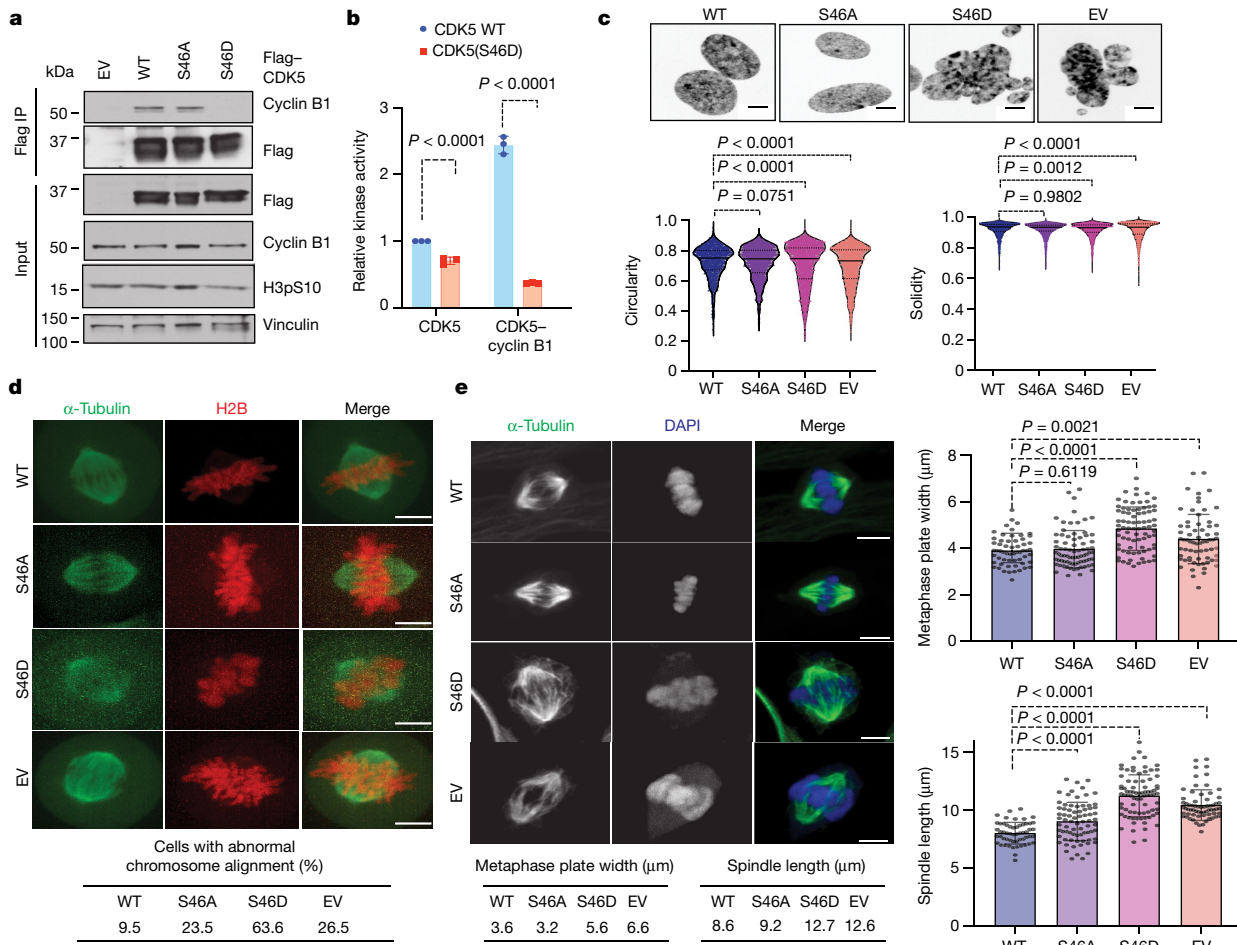


Fig. 5 | Disruption of the CDK5–cyclin B1 complex phenotypically recapitulates CDK5 abrogation. **a**, Immunoblots of Flag immunoprecipitation of the indicated Flag–CDK5 variants expressed in RPE-1, arrested in prometaphase by nocodazole treatment. Uncropped gel images are provided in Supplementary Fig. 1. **b**, Quantification of the relative kinase activity of the indicated immunoprecipitated CDK5 kinase complexes. Data are mean \pm s.d. from three independent experiments. **c**, Hoechst staining showing the nuclear morphology of RPE-1 CDK5(as) cells expressing the indicated Ser46 phosphovariants that were treated with 1NM-PP1 and fixed at 120 min after release from RO-3306-induced arrest at G2/M (top). Bottom, quantification of the nuclear circularity and nuclear solidity. **d**, Representative images of the final frame before the metaphase-to-anaphase transition from live-cell imaging experiments showing chromosome alignment at the metaphase plate of RPE-1 CDK5(as) cells treated with 1NM-PP1 and expressing the indicated Ser46 phosphovariants, mCherry–H2B and GFP– α -tubulin (top). Bottom,

quantification of the percentage of cells displaying abnormal chromosome alignment in metaphase. **e**, Representative images of RPE-1 CDK5(as) cells expressing the indicated Ser46 phosphovariants, treated with 1NM-PP1 before and after release from RO-3306-induced arrest into medium containing proTAME, and stained for α -tubulin and with DAPI (top left). Bottom left, measurements of metaphase plate width and spindle lengths of cells shown in the representative image. Right, quantification of metaphase plate width and spindle length after the indicated treatments. For **c**, data are mean \pm s.d. of three independent experiments from $n = 1,201$ (WT), $n = 1,993$ (S46A), $n = 2,444$ (S46D) and $n = 1,820$ (EV) cells. For **d** and **e**, data are mean \pm s.d. of at least two independent experiments from $n = 35$ cells for each treatment condition (**d**); and $n = 55$ (WT), $n = 75$ (S46A), $n = 81$ (S46D) and $n = 66$ (EV) (**e**) cells. *P* values were calculated using unpaired two-tailed Student's *t*-tests. Scale bars, 5 μm (**c–e**).

(Extended Data Fig. 8h), supporting our finding that CDK5 regulates spindle microtubule stability. These results demonstrate that, in contrast to CDK5 Ser159 regulating the activity of CDK5–p25 complex through its interaction with p25, it is regulating the activity CDK5–cyclin B1 complex through a distinct mechanism.

CDK5–cyclin B1 regulates mitotic fidelity

To ascertain whether CDK5–cyclin B1 forms a functional mitotic CDK complex to facilitate proper chromosome alignment and segregation, we mutated CDK5 residues that may disrupt its interaction with cyclin B1. The PSSALRE helix of CDK5 directly interacts with known activator p35/p25⁴⁸. Ser46 in the PSSALRE helix is conserved in CDK1 and CDK5 (Extended Data Fig. 9a,b) and can be phosphorylated⁵⁰. Immunoprecipitation of the phospho-null and phosphomimetic CDK5 variants at Ser46

showed that the phosphomimetic S46D variant reduced interaction with cyclin B1 (Fig. 5a). CDK5(S46D) exhibited minimal kinase activity due to its inability to interact and form active complex with cyclin B1 (Fig. 5b and Extended Data Fig. 9c). These results confirmed that the CDK5–cyclin-B1 complex is required for CDK5 kinase activity. To assess the impact of CDK5–cyclin-B1 complex on mitosis, we expressed the MYC–His-tagged Ser46 phosphovariants in RPE-1 CDK5(as) cells and inactivated CDK5(as) with 1NM-PP1 after mitotic entry, leaving the expressed Ser46 phosphovariant as the only functional CDK5 variant present during mitosis (Extended Data Fig. 9d). Expectedly, cells expressing CDK5(S46D) exhibited diminished levels of mitotic PP4R3 β Ser840 phosphorylation (Extended Data Fig. 9e,f). Compared with CDK5(as) cells expressing WT and S46A phospho-null variant, CDK5(as) cells expressing CDK5(S46D) and EV displayed nuclear abnormalities and decreased circularity and solidity (Fig. 5c). RPE-1 CDK5(as) cells

expressing EV and CDK5(S46D) also showed an increase in abnormal chromosome alignment (Fig. 5d, Extended Data Fig. 9g and Supplementary Videos 11–16), metaphase plate width and spindle length (Fig. 5e). These results indicated that expression of EV and CDK5(S46D) in RPE-1 CDK5(as) cells does not compensate for the loss of CDK5 activity, and these variants manifest the same phenotypes as CDK5 abrogation. We confirmed that Ser46 variants showed a similar localization pattern to wild-type CDK5 (Extended Data Fig. 10). Together, our results suggest that the CDK5–cyclin-B1 complex is essential for proper chromosome alignment and segregation. Disruption of the CDK5–cyclin-B1 complex phenocopies the mitotic defects observed after CDK5 ablation. Our results therefore establish the mitotic function of CDK5–cyclin-B1 complex in addition to the canonical CDK1–cyclin B1 complex in ensuring proper chromosome segregation.

Discussion

CDK5 functions in the nervous system² and is distinct from the classical cell-cycle-regulating CDK complexes as it is activated by the non-cyclin proteins p35 and p39 that are mainly expressed in post-mitotic neurons². Despite extraneuronal studies on CDK5^{17,18}, our understanding of CDK5 in the cell cycle remained incomplete as we could not inactivate CDK5 in a specific and temporally regulated manner. Here we used two independent chemical genetic approaches, the dTAG and analogue-sensitive systems, to overcome these impediments, revealing that the loss of CDK5 results in a higher rate of mitotic abnormalities, including defects in chromosome alignment, hyperstable spindle microtubules and impaired kinetochore–microtubule attachment error correction, leading to higher rates of chromosome mis-segregations and nuclear atypia after mitotic exit. We further recapitulated chromosome mis-segregation defects in 1NM-PP1-treated RPE-1 cells expressing CDK5(as) introduced by CRISPR knock-in, thereby confirming that the compromised mitotic fidelity after CDK5 inhibition by 1NM-PP1 is not due to overexpression of CDK5(as) (Extended Data Fig. 11). Phosphoproteomic analysis in the context of CDK5 inhibition identified putative CDK5 substrates in mitosis. Many of these factors are known to regulate microtubule stability and dynamics in mitosis and may contribute to the observed mitotic defects. It is very likely that a combination of multiple CDK5 substrates is responsible for the observed mitotic phenotype.

We conclusively demonstrate that CDK5 physically binds to and is activated by cyclin B1. We show that the CDK5–cyclin B1 complex is crucial for ensuring error-free mitosis, as the CDK5(S46D) variant that cannot bind to cyclin B1 is unable to compensate for the inhibition of the endogenous CDK5. CDK1–cyclin B1 has been established as the only CDK kinase that is required for mitosis. Our results revise this existing paradigm by demonstrating that CDK5–cyclin B1 is also required to ensure mitotic fidelity. The broader implication of our findings is that, in rapidly proliferating mammalian cells, there may be other CDK–cyclin complexes with unidentified roles that fine-tune the established cell-cycle-regulating CDKs attributed to different cell cycle phases.

Our phosphoproteomics analysis revealed that targets of CDK5 are also putative substrates of CDK1, suggesting functional redundancy between these two CDKs. This is not entirely surprising, as a recent publication showed that, in yeast, S-phase and mitotic CDKs have more functional overlap and less substrate specificity than was originally proposed¹³. Our results also suggest that there may be unique substrates of CDK5 that function in specific mitotic processes and enhance mitotic fidelity. For example, due to its enrichment on spindle microtubules during early stages of mitosis, CDK5 may have a more important role in the phosphorylation of microtubule-associated substrates and regulating microtubule dynamics. We speculate that post-translational modifications of cyclin B and/or differences in the precise temporal localization of the CDK5–cyclin B complex compared to CDK1–cyclin B might enable it to capture these unique substrates and confer unique function to each CDK complex. Building on our findings, future work

will dissect the differences between the CDK1 and CDK5 substrate specificities at different stages of mitosis.

While our study establishes the mitotic role of CDK5 in non-transformed cells, it also raises the possibility that CDK5–cyclin B1 may have an even larger role in the context of hyperproliferating cancer cells. As CDK5 overexpression is prevalent across a broad range of cancer types (Extended Data Fig. 12a), we speculate that certain cancers may exhibit an enhanced dependency on CDK5. To test plausibility of this hypothesis, we analysed the Cancer Cell Line Encyclopedia for dependencies on CDK1 and CDK5 and identified four tumour types of which cell lines showed enhanced dependency on CDK5 alongside diminished dependency on CDK1 (Extended Data Fig. 12b). Although these lines still rely substantially on CDK1, their dependency on CDK1 is comparatively lower and they exhibit a modestly increased dependency on CDK5. Notably, the reduced reliance on CDK1 correlates with elevated CDK5 expression (Extended Data Fig. 12c) and the proliferation rate of these tumour lines is positively correlated with CDK5 dependency (Extended Data Fig. 12d). These data lend further support to the pathophysiological role of CDK5 in cancer, underscoring the importance of future studies aimed at understanding the role of CDK5 in cancer progression and the development of CDK5-specific inhibitors. Together these observations transform our understanding of mitotic regulation in mammalian cells, compel us to revisit the longstanding designation of CDK5 as an atypical CDK and reinforce the therapeutic strategy to specifically target cancer cells dependent on CDK5 activity.

Online content

Any methods, additional references, Nature Portfolio reporting summaries, source data, extended data, supplementary information, acknowledgements, peer review information; details of author contributions and competing interests; and statements of data and code availability are available at <https://doi.org/10.1038/s41586-024-07888-x>.

- Wieser, S. & Pines, J. The biochemistry of mitosis. *Cold Spring Harb. Perspect. Biol.* **7**, a015776 (2015).
- Dhavan, R. & Tsai, L. H. A decade of CDK5. *Nat. Rev. Mol. Cell Biol.* **2**, 749–759 (2001).
- Malumbres, M. Cyclin-dependent kinases. *Genome Biol.* **15**, 122 (2014).
- Coverley, D., Laman, H. & Laskey, R. A. Distinct roles for cyclins E and A during DNA replication complex assembly and activation. *Nat. Cell Biol.* **4**, 523–528 (2002).
- Desai, D., Wessling, H. C., Fisher, R. P. & Morgan, D. O. Effects of phosphorylation by CAK on cyclin binding by CDC2 and CDK2. *Mol. Cell. Biol.* **15**, 345–350 (1995).
- Brown, N. R. et al. CDK1 structures reveal conserved and unique features of the essential cell cycle CDK. *Nat. Commun.* **6**, 6769 (2015).
- Strauss, B. et al. Cyclin B1 is essential for mitosis in mouse embryos, and its nuclear export sets the time for mitosis. *J. Cell Biol.* **217**, 179–193 (2018).
- Gavet, O. & Pines, J. Activation of cyclin B1-Cdk1 synchronizes events in the nucleus and the cytoplasm at mitosis. *J. Cell Biol.* **189**, 247–259 (2010).
- Barbiero, M. et al. Cell cycle-dependent binding between cyclin B1 and Cdk1 revealed by time-resolved fluorescence correlation spectroscopy. *Open Biol.* **12**, 220057 (2022).
- Pines, J. & Hunter, T. Isolation of a human cyclin cDNA: evidence for cyclin mRNA and protein regulation in the cell cycle and for interaction with p34cdc2. *Cell* **58**, 833–846 (1989).
- Clute, P. & Pines, J. Temporal and spatial control of cyclin B1 destruction in metaphase. *Nat. Cell Biol.* **1**, 82–87 (1999).
- Potapova, T. A. et al. The reversibility of mitotic exit in vertebrate cells. *Nature* **440**, 954–958 (2006).
- Basu, S., Greenwood, J., Jones, A. W. & Nurse, P. Core control principles of the eukaryotic cell cycle. *Nature* **607**, 381–386 (2022).
- Santamaria, D. et al. Cdk1 is sufficient to drive the mammalian cell cycle. *Nature* **448**, 811–815 (2007).
- Zheng, X. F. et al. A mitotic CDK5-PP4 phospho-signaling cascade primes 53BP1 for DNA repair in G1. *Nat. Commun.* **10**, 4252 (2019).
- Fagerberg, L. et al. Analysis of the human tissue-specific expression by genome-wide integration of transcriptomics and antibody-based proteomics. *Mol. Cell. Proteom.* **13**, 397–406 (2014).
- Pozo, K. & Bibb, J. A. The emerging role of Cdk5 in cancer. *Trends Cancer* **2**, 606–618 (2016).
- Sharma, S. & Sicinski, P. A kinase of many talents: non-neuronal functions of CDK5 in development and disease. *Open Biol.* **10**, 190287 (2020).
- Sun, K. H. et al. Novel genetic tools reveal Cdk5's major role in Golgi fragmentation in Alzheimer's disease. *Mol. Biol. Cell* **19**, 3052–3069 (2008).
- Sharma, S. et al. Targeting the cyclin-dependent kinase 5 in metastatic melanoma. *Proc. Natl Acad. Sci. USA* **117**, 8001–8012 (2020).

21. Nabet, B. et al. The dTAG system for immediate and target-specific protein degradation. *Nat. Chem. Biol.* **14**, 431–441 (2018).
22. Simpson, L. M. et al. Target protein localization and its impact on PROTAC-mediated degradation. *Cell Chem. Biol.* **29**, 1482–1504 e1487 (2022).
23. Vassilev, L. T. et al. Selective small-molecule inhibitor reveals critical mitotic functions of human CDK1. *Proc. Natl Acad. Sci. USA* **103**, 10660–10665 (2006).
24. Janssen, A. F. J., Breusegem, S. Y. & Larrieu, D. Current methods and pipelines for image-based quantitation of nuclear shape and nuclear envelope abnormalities. *Cells* **11**, 347 (2022).
25. Thompson, S. L. & Compton, D. A. Chromosome missegregation in human cells arises through specific types of kinetochore-microtubule attachment errors. *Proc. Natl Acad. Sci. USA* **108**, 17974–17978 (2011).
26. Kline-Smith, S. L. & Walczak, C. E. Mitotic spindle assembly and chromosome segregation: refocusing on microtubule dynamics. *Mol. Cell* **15**, 317–327 (2004).
27. Prosser, S. L. & Pelletier, L. Mitotic spindle assembly in animal cells: a fine balancing act. *Nat. Rev. Mol. Cell Biol.* **18**, 187–201 (2017).
28. Zeng, X. et al. Pharmacologic inhibition of the anaphase-promoting complex induces a spindle checkpoint-dependent mitotic arrest in the absence of spindle damage. *Cancer Cell* **18**, 382–395 (2010).
29. Warren, J. D., Orr, B. & Compton, D. A. A comparative analysis of methods to measure kinetochore-microtubule attachment stability. *Methods Cell. Biol.* **158**, 91–116 (2020).
30. Gregan, J., Polakova, S., Zhang, L., Tolic-Norrelykke, I. M. & Cimini, D. Merotelic kinetochore attachment: causes and effects. *Trends Cell Biol.* **21**, 374–381 (2011).
31. Etemad, B., Kuijt, T. E. & Kopf, G. J. Kinetochore-microtubule attachment is sufficient to satisfy the human spindle assembly checkpoint. *Nat. Commun.* **6**, 8987 (2015).
32. Tauchman, E. C., Boehm, F. J. & DeLuca, J. G. Stable kinetochore-microtubule attachment is sufficient to silence the spindle assembly checkpoint in human cells. *Nat. Commun.* **6**, 10036 (2015).
33. Mitchison, T. & Kirschner, M. Microtubule assembly nucleated by isolated centrosomes. *Nature* **312**, 232–237 (1984).
34. Fourest-Lievin, A. et al. Microtubule regulation in mitosis: tubulin phosphorylation by the cyclin-dependent kinase Cdk1. *Mol. Biol. Cell* **17**, 1041–1050 (2006).
35. Ubersax, J. A. et al. Targets of the cyclin-dependent kinase Cdk1. *Nature* **425**, 859–864 (2003).
36. Yang, C. H., Lambie, E. J. & Snyder, M. NuMA: an unusually long coiled-coil related protein in the mammalian nucleus. *J. Cell Biol.* **116**, 1303–1317 (1992).
37. Yang, C. H. & Snyder, M. The nuclear-mitotic apparatus protein is important in the establishment and maintenance of the bipolar mitotic spindle apparatus. *Mol. Biol. Cell* **3**, 1259–1267 (1992).
38. Kotak, S., Busso, C. & Gonczy, P. NuMA phosphorylation by CDK1 couples mitotic progression with cortical dynein function. *EMBO J.* **32**, 2517–2529 (2013).
39. Kitagawa, M. et al. Cdk1 coordinates timely activation of MKlp2 kinesin with relocation of the chromosome passenger complex for cytokinesis. *Cell Rep.* **7**, 166–179 (2014).
40. Schrock, M. S. et al. MKLP2 functions in early mitosis to ensure proper chromosome congression. *J. Cell Sci.* **135**, jcs259560 (2022).
41. Sun, M. et al. NuMA regulates mitotic spindle assembly, structural dynamics and function via phase separation. *Nat. Commun.* **12**, 7157 (2021).
42. Chen, Q., Zhang, X., Jiang, Q., Clarke, P. R. & Zhang, C. Cyclin B1 is localized to unattached kinetochores and contributes to efficient microtubule attachment and proper chromosome alignment during mitosis. *Cell Res.* **18**, 268–280 (2008).
43. Kabche, L. & Compton, D. A. Cyclin A regulates kinetochore microtubules to promote faithful chromosome segregation. *Nature* **502**, 110–113 (2013).
44. Hegarat, N. et al. Cyclin A triggers mitosis either via the Greatwall kinase pathway or cyclin B. *EMBO J.* **39**, e104419 (2020).
45. Jumper, J. et al. Highly accurate protein structure prediction with AlphaFold. *Nature* **596**, 583–589 (2021).
46. Wood, D. J. & Endicott, J. A. Structural insights into the functional diversity of the CDK-cyclin family. *Open Biol.* **8**, 180112 (2018).
47. Brown, N. R., Noble, M. E., Endicott, J. A. & Johnson, L. N. The structural basis for specificity of substrate and recruitment peptides for cyclin-dependent kinases. *Nat. Cell Biol.* **1**, 438–443 (1999).
48. Tarricone, C. et al. Structure and regulation of the CDK5-p25^{nck5a} complex. *Mol. Cell* **8**, 657–669 (2001).
49. Poon, R. Y., Lew, J. & Hunter, T. Identification of functional domains in the neuronal Cdk5 activator protein. *J. Biol. Chem.* **272**, 5703–5708 (1997).
50. Oppermann, F. S. et al. Large-scale proteomics analysis of the human kinome. *Mol. Cell. Proteom.* **8**, 1751–1764 (2009).

Publisher's note Springer Nature remains neutral with regard to jurisdictional claims in published maps and institutional affiliations.

Springer Nature or its licensor (e.g. a society or other partner) holds exclusive rights to this article under a publishing agreement with the author(s) or other rightsholder(s); author self-archiving of the accepted manuscript version of this article is solely governed by the terms of such publishing agreement and applicable law.

© The Author(s), under exclusive licence to Springer Nature Limited 2024

Methods

Reagents

Urea (U0631), Trizma base (T2694), ammonium hydroxide solution (320145), ammonium bicarbonate (NH4HCO3, A6141), EGTa (E0396), EDTA (E7889), iodoacetamide (IAM, A3221), trifluoroacetic acid (TFA, 302031), protease inhibitor cocktail (P8340) and phosphatase inhibitor cocktails #3 (P0044) and #2 (P5726) were obtained from Sigma-Aldrich. Acetonitrile (A955), water (W6, LCMS Optima grade), tris(2-carboxyethyl) phosphine (TCEP, 77720) and TMT11plex isobaric label reagent set (TMT, 34808) were obtained from Thermo Fisher Scientific. Formic acid (1.11670.1000) was obtained from EMD Millipore. Lys-C (Wako, 129-02541) and sequencing-grade trypsin (Promega, V5111) were used for digestion of samples.

Antibodies

The antibodies used in this study were as follows: mouse α-tubulin (B-7, Santa Cruz, sc-5268, 1:500 for immunoblotting (IB) and immunofluorescence (IF)), mouse β-actin (C4, Santa Cruz, sc-47778, 1:500, IB), rabbit CDK1 (EPR165, ab133327, 1:10,000, IB and IF), mouse CDC2 p34 (sc-54 AC, 25 µl slurry used per mg of lysate for immunoprecipitation (IP)), mouse CDK2 (D-12, Santa Cruz, sc-6248, 1: 500, IB), rabbit CDK5 (EP715Y, Abcam, ab40773, 1:200 for IF, 1:1,000 for IB), mouse CDK5 (J-3, Santa Cruz, sc-6247, 1:500, IB), mouse CDK5 (DC 17, Santa Cruz, sc-249 AC, 25 µl slurry used per mg of lysate for IP), human anti-centromere (Centromere Antibodies, 15-235, 1:500, IF), mouse MYC (9E10, Santa Cruz, sc-40, 1:500, IB), rabbit MYC (Y69, Abcam, ab32072, 1:100 for IF, 1:500 for IB, 2.5 µg for IP), rabbit cyclin A2 (Novus Biologicals, NBP131330, 1:500, IB), rabbit cyclin B1 (Y106, Abcam, ab32053, 1:200, IF), rabbit cyclin B1 (Abcam, ab2949, 1:1,000, IB), mouse cyclin B1 (GNS1, Santa Cruz, sc-245, 1:500 for IB, 1:400 for IF), mouse cyclin B1 (D-1, Santa Cruz, sc-166210 AC, 25 µl slurry used per mg of lysate for IP), mouse Flag (Sigma-Aldrich, F1804, 1:1,000, IB), rabbit Flag (Bethyl, A190-102A, 1:1,000, IB), rabbit HA-Tag (C29F4, Cell Signaling Technology, 3724, 1:500, IB), rabbit KIF20A/RAB6KIFL (Thermo Fisher Scientific, 501730568, 1:1,000, IB), normal rabbit IgG (Cell Signaling Technology, 2729S, 5 µl used per IP), normal mouse IgG (Santa Cruz, SC-2025, 5 µl used per IP), mouse NUMA1 (Life Technologies, MA5-17293, 1:500, IB, IF), rabbit p35/25 (C64B10, Cell Signaling Technology, 2680, 1:500, IB), mouse p35 (4G11, Santa Cruz, sc-293184, 1:1,000, IB), rabbit p39 EPR5074 (Abcam, ab124896, 1:1,000, IB), rabbit phospho-CDK5 (Ser159, Life Technologies, PA564751, 1:500, IB), rabbit phospho-histone H3 (Ser10, Cell Signaling Technology, 9701, 1:500, IB), phospho-Ser/Pro antibody: rabbit phosphorylated (Ser) CDK substrate (P-S2-100, Cell Signaling Technology, 9477S, 10 µl was used per IP), rabbit PP4R3/SMEK2 (Abcam, Ab224222, 1:50, IF), PP4R3β/SMEK2 rabbit phospho-S840 (GL Bio-chem, custom made, 1:100, IF) and mouse vinculin (H-10, Santa Cruz, sc-25336, 1:1,000, IB).

Cell line sources, plasmid construction and generation of stable cell lines

293T, HeLa and RPE-1 were obtained from and validated by short tandem repeat (STR) genotyping at ATCC. Modified cell lines (CRISPR knockout, CDK5 variant overexpressing lines) created for this study are described in details below. Modified cell lines were confirmed by immunoblotting and/or genomic sequencing. All cell lines were tested negative for mycoplasma using MycoAlert Plus Mycoplasma Detection Kit (Lonza, LT07). The CDK5 CRISPR targeting sequence and the sequence of the guide RNA to remove endogenous CRISPR knockout were described previously¹⁵. Human CDK5 cDNA⁵¹ (Addgene, 1872) was mutagenized to the CRISPR guide-resistant variant using site-directed mutagenesis by PCR using the following primers: Forward, 5'-GCCAAAAACCGGGAACTCATGAGATTGTGGCTCTGAAACGG; reverse, 5'-CCGTTTCAGAGCCACAATCTCATGAGTTCCCGGTTTTGGC.

RPE-1 expressing Flag-HA-CDK5(as) variant. The CDK5 analogue-sensitive variant was generated by mutagenizing phenylalanine-80 to glycine (F80G) using site-directed mutagenesis on a plasmid containing guide-resistant CDK5 described above, by PCR using the following primers: forward, 5'-GACAAGAAGCTGACTTTGGTGGGGA ATTCTGTGACCAGGACCTG; reverse, 5'-CAGGTCTGGTCACAGA ATTCCCCAACCAAAGTCAGCTTCTGTC.

Guide-resistant CDK5 WT and CDK5(as) were subcloned into the NotI site of the pOZ-N terminal Flag-HA vector by PCR using the following primers: forward, 5'-AATTCGCGGCCCTGCAGAAAT ACGAGAAACTGGAAAAGATTGGGAAGGCACC; reverse, 5'-AACAG CGGCCGCTAGGGCGGACAGAAGTCGGAGAAGTAGGG.

RPE-1 cells stably expressing the pOZ Flag-HA-CDK5(as) variant were created by retroviral production and transduction. Retroviral production was performed using HEK293T Phoenix cells, which were co-transfected with pUMVC3-gag-pol, pCMV-VSVG/pCCEnv (Addgene, 8454), and pOZ-Flag-HA-CDK5(WT) or pOZ Flag-HA-CDK5(as) retroviral plasmids using Lipofectamine 3000 (Thermo Fisher Scientific, L300001S) according to the manufacturer's instructions. Viral particles were collected 48 h after transfection and filtered through a 0.45 µM membrane syringe filter (Thermo Fisher Scientific, 723-2545). Filtered viral supernatant was applied to RPE-1 cells in the presence of 8 µg ml⁻¹ polybrene (Sigma-Aldrich, 107689). As the pOZ is a retroviral vector that contains a bicistronic transcriptional unit that allows expression of the gene of interest (CDK5(as)) and the interleukin-2 receptor chain (IL-2Ra), a selection marker⁵², transduced RPE-1 cells were selected by Dynabeads CD25, or anti-IL-2Ra-antibody-conjugated magnetic beads (Thermo Fisher Scientific, 11157D). Endogenous CDK5 was subsequently removed from RPE-1 expressing CDK5(as) by CRISPR guide-mediated knockout. Specifically, 37.5 pmol of CDK5 guide RNA and 37.5 pmol of TrueCut Cas9 (Thermo Fisher Scientific, A36497) were transfected into RPE-1 cells expressing CDK5(as) using Lipofectamine CRISPRMAX Cas9 Transfection Reagent (Invitrogen, CMAX00008) according to the manufacturer's instructions. Transduced RPE-1 CDK5(as) cells with endogenous CDK5 removed by CRISPR-Cas9 were then sorted as a single cell per well in a 96-well plate. Sorting was performed at the Dana-Farber Cancer Institute Core Flow Cytometry facility on the M Aria II system, through a 100 µm nozzle into DMEM-F12 medium containing 50% FBS. Single-cell clones were verified for expression of Flag-HA-CDK5(as) and removal of endogenous CDK5 by immunoblotting, as shown in Extended Data Fig. 1b.

RPE-1 cells expressing the HA-CDK5(dTAG) variant. To generate the construct expressing N-terminal dTAG fused to guide-resistant CDK5, or FKBP^{F36V}-HA-CDK5, guide-resistant CDK5 was subcloned into lentiviral plasmid pLEX_305-N-dTAG (Addgene, 91797)²¹ by Gateway recombination cloning technology (Invitrogen). Guide-resistant CDK5 was first subcloned from pOZ into the Gateway-compatible donor vector pDONR223 using the Gateway BP Clonase II Enzyme mix (Invitrogen, 11789) after PCR using primers containing BP overhang: forward, 5'-GGGGACAACCTTGACAAAAAGTTG GCCAGAAATACGAGAAACTGGAAAAGATTGGGG; reverse, 5'-GG GGACAACTTGTACAAGAAAGTTGGCTAGGGCGGACAGAAGTCGG AGAAG.

Then, 150 ng of pDONR223 containing CDK5 was mixed with 150 ng of pLEX_305-N-dTAG in 10 µl. Next, 2 µl of LR clonase II enzyme mix (Life Technologies) was added to the plasmid mix and incubated for 1 h at room temperature. Then, 1 µl of proteinase K (Thermo Fisher Scientific, EO0491) was added to terminate the reaction and incubated at 37 °C for 10 min. The reaction mixture was transformed using Stbl3-competent cells, plated onto Ampicillin-selective medium and grown at 30 °C. Plasmid DNA was purified using the QIAprep Spin Miniprep Kit (Qiagen, 27106) and insertions were confirmed by BsrGI-HF (New England Biolab, R0575) and gel electrophoresis. Plasmids were sequenced using following

Article

primers: hPGK forward: 5'-GTGTTCCGCATTCTGCAAG; WPRE reverse: 5'-CATAGCGTAAAGGAGCAACA.

RPE-1 cells stably expressing CDK5(dTAG) were created by lentiviral production and transduction. Lentiviral production was performed using HEK293T cells, which were co-transfected with pMD2.G (Addgene, 12259), psPAX2 (Addgene, 12260) and dTAG lentiviral plasmids using Lipofectamine 3000 (Thermo Fisher Scientific, L3000015), according to the manufacturer's instructions. Viral particles were collected 48 h after transfection and filtered through a 0.45 μm membrane syringe filter (Thermo Fisher Scientific, 723-2545). Filtered viral supernatant was applied to RPE-1 cells in the presence 8 $\mu\text{g ml}^{-1}$ polybrene (Sigma-Aldrich, 107689). Transduced RPE-1 cells were selected with 10 $\mu\text{g ml}^{-1}$ puromycin for 2 weeks. Endogenous CDK5 was subsequently removed from RPE-1 cells expressing CDK5(dTAG) by CRISPR guide-mediated knockout, as done for RPE-1 CDK5(as) cells described above. Transduced RPE-1 cells expressing CDK5(dTAG) with endogenous CDK5 removed by CRISPR–Cas9 were then sorted into a single cell per well of a 96-well plate as was done for RPE-1 CDK5(as) cells described above. Single-cell clones were verified for expression of HA-dTAG and removal of endogenous CDK5 by immunoblotting, as shown in Extended Data Fig. 2b.

RPE-1 CDK5(as) and RPE-1 CDK5(dTAG) cells expressing mCherry–H2B and GFP– α -tubulin for live-cell imaging. RPE-1 CDK5(as) and RPE-1 CDK5(dTAG) cells stably expressing mCherry–H2B and GFP– α -tubulin were created by lentiviral production and transduction. Lentiviral production was performed using HEK293T cells, which were co-transfected with pMD2.G (Addgene, 12259), psPAX2 (Addgene, 12260) and lentiviral plasmid pLenti6-H2B-mCherry (Addgene, 89766) or lentiviral plasmid pL304-eGFP- α -tubulin (Addgene, 64060) using Lipofectamine 3000, as described above. Viral particles containing mCherry–H2B or GFP– α -tubulin were filtered as described as above and applied at a 1:1 ratio to RPE-1 CDK5(as) or RPE-1 CDK5(dTAG). Transduced cells were then sorted to isolate population expressing mCherry–H2B and GFP–tubulin at 50% intensity, using fluorochrome 530/30 for GFP and 610/20 for mCherry, through a 100 μm nozzle, into 10 ml DMEM-F12 medium containing 50% FBS.

RPE-1 stably expressing Flag–HA–CDK5 phosphovariants. CDK5 Ser46 and Ser159 phosphovariants in pOZ Flag-HA were created using site-directed mutagenesis by PCR with the following primers: S46A forward: 5'-GATGAGGGTGTGCCGGCTCCGCCCTCCGGGAGATCTGC; S46A reverse: 5'-GCAGATCTCCCGAGGGCGGAAGCCGGCACAC CCTCATC; S46D forward: 5'-GATGAGGGTGTGCCGGATTCCGCCCT CCGGGAGATCTGC; S46D reverse: 5'-GCAGATCTCCCGAGGGCG GAATCCGGCACACCCTCATC; S159A forward: 5'-GATTCCCGTCCGCTG TTACGCAGCTGAGGTGGTCACACTG; S159A reverse: 5'-CAGTGTGAC CACCTCAGCTCGTAACAGCGGACGGGAATC.

RPE-1 cells stably expressing Flag–HA–CDK5 phosphovariants were generated using retroviral production and transduction, as done for RPE-1 CDK5(as), described above.

RPE-1 CDK5(as) cells expressing His–MYC–CDK5 phosphovariants. Guide-resistant CDK5 Ser46 phosphovariants and/or S159 phosphovariants generated above were subcloned from pOZ-Flag-HA into the NotI and XbaI sites of the vector pCDNA3.1-HisA-6xmyc¹⁵ using the following primers: forward, AGCACAGTGGCGCCGCTCAGAAATACGA GAAACTG; reverse, CCTCTAGACTCGCTAGGGCGGACAGAACGTCGGAG.

pCDNA3.1-HisA-6xmyc containing CDK5WT, S46A, S46D and S159A were transfected into RPE-1 CDK5(as) cells using Lipofectamine 3000, according to the manufacturer's instructions. Cells expressing His–MYC–CDK5 Ser46 or Ser159 phosphovariants were selected by 500 $\mu\text{g ml}^{-1}$ G-418 or geneticin (Goldbio, G-418-S) and single-cell sorted as described above. Single-cell clones were verified for expression of His–MYC–CDK5 Ser159 or Ser46 phosphovariants by immunoblotting

as shown in Extended Data Fig. 8d,e and Extended Data Fig. 9d, respectively.

RPE-1 CDK5(as) cells expressing Ser46 phosphovariants or Ser159 phosphovariants expressing mCherry–H2B and GFP– α -tubulin for live-cell imaging. These cell lines were created by lentiviral production and transduction, as was done for RPE-1 CDK5(dTAG) and RPE-1 CDK5(as) expressing mCherry–H2B and GFP– α -tubulin. Viral particles containing mCherry–H2B or GFP– α -tubulin were filtered as described as above and applied at a 1:1 ratio to RPE-1 CDK5(as) cells expressing His–MYC-tagged Ser46 phosphovariants or Ser159 phosphovariants.

RPE-1 CDK5(F80G)-as knock-in. RPE-1 cells were transfected with guide: 5'-CAGCGACAAGAACUGACUU; single-stranded oligo-deoxynucleotides (ssODN) or donor template: 5'-GCTTCATGACGTCCTGCA CAGCGACAAGAACGCTGACCTGGTGGTAATTCTGTGACCAGGTGA AAGGCCGGGTTTGA; and TrueCut Cas9 v2 using Lipofectamine CRISPRMAX Cas9 Transfection Reagent (Thermo Fisher Scientific, CMAX00008). Immediately before applying the transfection mixture, fresh medium containing 20 μM DNA ligase IV inhibitor SCR7 (Sigma-Aldrich, SML1546) was applied to the cells. Then, 48 h after transfection, transfected cells were trypsinized and reseeded in fresh medium without SCR7. Next, 96 h after transfection, cells were single-cell-sorted into 96-well plates. The knock-in efficiency was verified by next-generation sequencing of amplicons generated using forward PCR primer: 5'-TGAGCCCTTCTTTGCCCTA; and reverse PCR primer: 5'-CAACACCACTCTCCTCACCT from genomic DNA of the transfected cell pool, extracted using the DNeasy Blood and Tissue Kit (Qiagen, 69504). Amplicon was resolved by gel electrophoresis on a 2% agarose gel, purified by gel purification (Qiagen, 28706) and quantified in Qubit Assay Tubes (Thermo Invitrogen Q32856) using the Qubit dsDNA HS Assay kit (Thermo Invitrogen, Q32851) using the Qubit 4 Fluorometer. Individual clones were verified for CDK5(as)/F80G knock-in by Sanger sequencing of the PCR product, amplified by the PCR primers described above.

Cell culture

All cells were cultured at 37 °C under a 5% CO₂ atmosphere with 100% humidity. HeLa and HEK293T cells were cultured in DMEM with high glucose and pyruvate (Invitrogen, 11995-065) supplemented with 10% (v/v) FBS (Invitrogen, 10437028) and 1% penicillin–streptomycin (Invitrogen, 15140-122). Telomerase-immortalized (hTERT) RPE-1 cells were cultured in DMEM-F12 medium (Invitrogen, 21041-065) containing 10% FBS and 1% penicillin–streptomycin. Inhibition of CDK5(as) was achieved by adding 2.5 μM of 1NM-PPI. Degradation of CDK5(dTAG) was achieved by adding 0.5 μM of dTAG-13.

Cell cycle synchronization

For synchronization to G2/M, cells were treated with RO-3306²³ at a final concentration of 9 μM for 16–18 h. For synchronization to pro-metaphase, cells were treated with nocodazole (Sigma-Aldrich, M1404) at a final concentration of 100 ng ml⁻¹ for 6 h. Cells were released from RO-3306-mediated G2/M arrest by washing five times with prewarmed 1× PBS (Corning, 21-040) before adding fresh medium. Cells were released from nocodazole-mediated prometaphase arrest by mitotic shake-off and washing four times with prewarmed fresh medium. For synchronization to metaphase, cells were at first arrested in G2/M by treatment with RO-3306, cells were then washed and released into medium containing 20 μM of proTAME (Medchem Express, HY-124955) for 2 h.

Cell proliferation or growth curve

A total of 30,000 cells was seeded per well in a six-well plate on day 0. On the day of counting, cells in all of the wells were washed with prewarmed PBS, trypsinized in 0.5 ml of 0.05% trypsin-EDTA (Gibco, 25200114) and

resuspended in 1 ml of medium. Then, 10 µl of cell suspension was used for counting on the Countess 3 Automated Cell Counter (Invitrogen, AMQAX2000).

Immunofluorescence microscopy

Cells released from synchronization described above were fixed with 4% paraformaldehyde (Electron Microscopy Sciences, 15710) for 15 min. Fixed samples were washed with PBS, permeabilized for 5–10 min at room temperature with PBS with 0.5% Triton X-100 and washed with PBS. The samples were then blocked in PBS with 3% BSA (Sigma-Aldrich, 10735086001) for 1 h and incubated with primary antibodies diluted in blocking buffer overnight. The samples were washed three times with PBS with 0.05% Triton X-100, incubated with secondary antibodies diluted in blocking buffer at room temperature for 1 h and washed again three times in PBS with 0.05% Triton X-100. DNA was stained using Hoechst for 20 min, washed and mounted in ProLong Gold antifade (Life Technologies) on glass slides. Alternatively, after washing following the secondary antibody incubation, the samples were washed once in Ultrapure Distilled Water (Invitrogen, 10977) before being invert-mounted onto glass slides.

Imaging was performed on a spinning-disk confocal microscope (a Nikon Ti2 with a Yokogawa CSU-W1 spinning-disk head). z-stack images at 0.5 µm spacing were collected with a ×60/1.40 NA Plan Apochromat oil-immersion objective (Nikon).

Image and nuclear shape analysis

For fixed cells, images were acquired with either a ×20 or ×60 objective as described above. Quantitative analysis of these images was performed using ImageJ/Fiji. The region of interest (ROI) was either manually drawn around cell boundaries (for ×60 mitotic cells) or defined using image segmentation (for ×20 primary nuclei). For nuclear segmentation, either Li or Otsu thresholding was used on maximum-intensity projections of z-stacks of images acquired using 405 nm laser (DAPI-stained). Second, after the images were converted into binary, the objects (nuclei) were processed using the Erode and Dilate processing tools in ImageJ/Fiji. Lastly, we separated the clumped nuclei using Watershed Spatial Analyst program (ArcGIS Pro v.3.3). The ROIs generated were then overlayed on the 405 nm images and used to measure circularity and solidity using ImageJ/Fiji shape descriptor tools. For measuring nuclear parameters, cells were imaged with a ×20 objective in 8 × 8 tiles. The tiles were stitched and at least 200 cells were analysed per image. Lobular, fragmented (including ‘bunch-of-grapes’) nuclei or nuclei containing blebs, folds and/or crevices were manually scored as abnormal nuclei. For quantification of the fluorescence intensity of labelled proteins, ROIs were defined as described above and either the total (mean × total area) or normalized intensity was determined in the indicated channel after background subtraction (determined from the ROI outside the cell). Normalization was performed to total DAPI intensity. The Manders’ overlap coefficients were derived using the JACoP Fiji tool for colocalization analysis. The thresholding was kept constant throughout the images analysed.

Live-cell imaging

Live-cell imaging videos were performed and analysed using NIS-Elements (Nikon). To perform live-cell imaging, cells were stably expressed with both mCherry-H2B and GFP-tubulin to capture mitotic events. Live-cell imaging was performed on the Ti2 inverted microscope fitted with a CSU-W1 spinning-disk system (Nikon). To capture mitotic cells, z-stacks (+6 (above) and –4 (below) planes at 0.5 µm spacing) were captured every 2 min for 2–4 h, using a Zyla 4.2 sCMOS camera (Andor), and a 20×/0.95 NA Plan Apochromat Lambda objective with the correction collar set to 0.17. For higher-resolution imaging of cells undergoing mitosis, imaging was performed on the Nikon Ti2 inverted microscope fitted with a Yokogawa CSU-W1 spinning-disk head. z-stacks (+6 (above) and –4 (below) at 0.75 µm spacing) were collected every

2 min for 2 h, using the CoolSnap HQ2 CCD camera (Photometrics), and the ×100/1.45 NA Plan Apochromat Lambda oil-immersion objective (Nikon). An environmental enclosure was used to maintain cell culture conditions (37 °C and humidified 5% CO₂) for all live-cell confocal imaging. The timing of mitosis was measured from the point of DNA condensation to the onset of anaphase. The spindle geometry was determined in metaphase cells before the onset of anaphase.

Spindle geometry, IKD and cold-shock assays

RPE-1 CDK5(as) or RPE-1 CDK5(dTAG) cells were treated with 9 µM of RO-3306 for 18 h to arrest cells at the G2/M border. Then, 2 h before release, RPE-1 CDK5(as) and RPE-1 CDK5(dTAG) cells were treated with either DMSO or 1NM-PP1 or dTAG-13 to inhibit or degrade CDK5 in the respective cell line. Next, 18 h after initial RO-3306 treatment, the cells were released from G2/M arrest by washing with prewarmed medium four times and adding fresh medium containing 20 µM pro-TAME and DMSO, 1NM-PP1 or dTAG-13 for 2 h for the spindle geometry and IKD experiments. The cells were then fixed with 3.5% of PFA and immunostained as described above. For the cold-shock assay, the cells were released from G2/M arrest by washing four times with prewarmed medium into fresh medium containing 5 µM MG-132 and DMSO, 1NM-PP1 or dTAG-13 for 2 h. The cell culture dish was then placed on ice for 30 min. The cells were then fixed with cold methanol for 10 min on ice and immunostained as described above. The IKD and cold-shock assay were performed and analysed as previously described²⁹.

Protein extraction and immunoblotting

Protein extracts were prepared in NETN buffer (50 mM Tris pH 7.5, 1 mM EDTA, 0.5% NP-40, 5% glycerol, 150 mM NaCl, cOmplete EDTA-free protease inhibitor cocktail (Sigma-Aldrich, 1183617001) and PhosSTOP phosphatase inhibitor cocktail (Sigma-Aldrich, 04906837001)). In brief, cells were collected and washed three times in ice-cold PBS before resuspending in lysis buffer. After incubation for 20 min with end-over-end rotation at 4 °C, the cell lysate was clarified by centrifuging at 13,000 rpm for 10 min. The protein concentration in clarified lysate was determined using the Pierce BCA Protein Assay Kit (Thermo Fisher Scientific, 23225) with reference to a standard curve generated with BSA. Extracts were mixed with 4× Laemmli sample buffer and heated at 95 °C for 5 min. Denatured extracts were resolved on pre-cast NuPAGE 4–12%, 1.5 mm Bis-Tris polyacrylamide gels (Life Technologies, NP0335) and transferred to 0.2 µm nitrocellulose membranes (BioRad, 1620112). The membranes were blocked in 5% BSA (Sigma-Aldrich, 10735086001) in TBS-1% Tween-20 for 1 h and incubated in primary antibodies at 4 °C for 16–18 h. The membranes were washed three times the next day with TBS-0.05% Tween-20 at room temperature with rocking. Membranes were probed with HRP-conjugated goat anti-mouse (Jackson ImmunoResearch, 115035008) or goat anti-rabbit (Jackson ImmunoResearch, 111035008) antibodies for 1 h (1:3,000). The Amersham ECL Western Blotting Detection Reagent Kit (GE Healthcare, RPN2106) was used to develop the blots. Blots were developed using Cytiva ImageQuant 800.

Phospho-proteomics MS and data analysis

Protein lysate preparation. RPE-1 CDK5(as) or RPE-1 CDK5(dTAG) were arrested at G2/M with 9 µM of RO-3306 for 16 h to arrest cells at the G2/M border. Then, 2 h before release, RPE-1 CDK5(as) and RPE-1 CDK5(dTAG) cells were treated with 1NM-PP1 or dTAG-13 to inhibit or degrade CDK5 in the respective cell line. Next, 18 h after the initial RO-3306 treatment, the cells were released from G2/M arrest by washing four times with prewarmed PBS and adding fresh medium containing DMSO, 1NM-PP1 or dTAG-13 for continuing abrogation of CDK5 as cells progress through mitosis. At 50 min after release from RO-3306 arrest, mitotic cells were collected by shake-off and kept on ice. Mitotic cells were washed in ice-cold PBS three times and pelleted by centrifugation at 1,400 rpm for 6 min. The cells were lysed in urea lysis buffer

Article

(6 M urea, 25 mM Tris pH 8.0, 1 mM EDTA, 1 mM EGTA with protease inhibitor (Sigma-Aldrich, P8340), phosphatase cocktail 2 (Sigma-Aldrich, P8340) and 3 (Sigma-Aldrich, P0044)). The lysates were passed through a 26-gauge needle and syringe six times on ice to shear chromatin before clarifying by centrifugation at 14,000 rpm for 10 min. The lysates were transferred to a chilled cryovial and rapidly frozen down by liquid nitrogen and stored in -80 °C before downstream processing.

Protein digestion. Protein was quantified in lysates using the Micro BCA Assay (Thermo Fisher Scientific), and the lysates were diluted to 1.28 mg ml⁻¹ using lysis buffer. Lysates were reduced in 23.8 mM TCEP (Thermo Fisher Scientific) for 30 min at 37 °C with shaking, followed by alkylation with 56.3 mM iodoacetamide (Sigma-Aldrich) in the dark at room temperature for 30 min. The lysates were then diluted with 1.69 ml 200 mM Tris (pH 8.0). Lys-C (Wako) was dissolved in 25 mM Tris (pH 8.0) at 400 µg ml⁻¹ and added to lysates at 1:100 (enzyme:protein) ratio by mass and incubated for 2 h at 37 °C with shaking. The lysates were then diluted with 1.485 ml 200 mM Tris (pH 8.0) and trypsin was added at a 1:50 trypsin:protein ratio and incubated for 3.5 h at 37 °C with shaking. After 3.5 h, a second trypsin aliquot was added at a 1:100 trypsin:protein ratio. Digestion was carried out overnight at 37 °C with shaking. After 16 h, the reaction was quenched with formic acid to a final concentration 1% by volume. The samples were desalted using Oasis HLB 96-well plates (Waters) and a positive pressure manifold (Waters). The plate wells were washed three times with 400 µl of 50% acetonitrile/0.1% formic acid, and then equilibrated four times with 400 µl of 0.1% formic acid. The digests were applied to the wells, then washed four times with 400 µl 0.1% formic acid before being eluted drop by drop three times with 400 µl of 50% acetonitrile/0.1% formic acid. The eluates were lyophilized, followed by storage at -80 °C until use.

Isobaric labelling. Global phospho-profiling samples were labelled with the TMT11plex isobaric label reagent set (TMT; Thermo Fisher Scientific, 34808). Desalted peptides were resuspended in 50 mM HEPES at 1 mg ml⁻¹ based on starting protein mass. TMT reagents were resuspended in 256 µl acetonitrile and transferred to the peptide sample. The samples were incubated at room temperature for 1 h with mixing. Labelling reactions were quenched by the addition of 50 µl of hydroxy-lamine (Sigma-Aldrich, 438227) diluted to 5% in H₂O and incubated for 15 min at room temperature with mixing. The independent labelling reactions were then pooled together and lyophilized. The labelled peptides were desalted as described above and then lyophilized and stored at -80 °C.

Basic (high pH) reverse-phase LC. The desalted tryptic digest was fractionated by high-pH reverse phase liquid chromatography. In total, 5.5 mg of the protein digest was loaded onto the liquid chromatography (LC) system consisting of the Agilent 1200 HPLC (Agilent) system with mobile phases of 5 mM NH₄HCO₃, pH 10 (A) and 5 mM NH₄HCO₃ in 90% acetonitrile, pH 10 (B). The peptides were separated by a 4.6 mm × 250 mm Zorbax Extend-C18, 3.5 µm, column (Agilent, 770953-902) over 96 min at a flow rate of 1.0 ml min⁻¹ by the following time schedule: hold 0% B for 9 min, gradient from 0 to 10% B for 4 min, 10 to 28.5% B for 50 min, 28.5 to 34% B for 5.5 min, 34 to 60% B for 13 min, hold at 60% B for 8.5 min, 60 to 0% B for 1 min, re-equilibrate at 0% B for 5 min. 1 min fractions were collected from 0–96 min by the shortest path by row in a 1 ml deep well plate (Thermo Fisher Scientific, 95040450). The high-pH reverse-phase fractions were concatenated into 24 samples by every other plate column (for example, sample 1 contained fractions from wells A1, C1, E1 and so on). 95% of every 12th fraction of the 24 samples was combined (1,13; 2,14 and so on) to generate 12 samples, which were dried down and stored at -80 °C before phosphopeptide enrichment.

Immobilized metal affinity chromatography. For discovery LC-MS/MS analysis, fractionated samples were enriched for phosphopeptides by immobilized metal affinity chromatography. Enrichment was performed using Ni-NTA-agarose beads (Qiagen, 36113) stripped with EDTA and incubated in a 10 mM FeCl₃ solution to prepare Fe³⁺-NTA-agarose beads. Peptide samples were reconstituted in 200 µl of 0.1% TFA in 80% acetonitrile and incubated for 30 min with 100 µl of the 5% bead suspension, mixing at 1,400 rpm at room temperature. After incubation, the beads were washed three times with 300 µl of 0.1% TFA in 80% acetonitrile. Phosphorylated peptides were eluted from the beads using 200 µl of 70% acetonitrile, 1% ammonium hydroxide for 1 min with agitation at room temperature (do not exceed 5 min). The samples were transferred into a fresh tube containing 60 µl of 10% formic acid, dried down and resuspended in 0.1% formic acid, 3% acetonitrile. The samples were frozen at -80 °C until analysis.

Nano-LC-MS/MS. Phosphopeptide-enriched samples were analysed using LC-MS/MS on the Easy-nLC 1000 (Thermo Fisher Scientific) system coupled to an Orbitrap Eclipse Tribrid mass spectrometer (Thermo Fisher Scientific) operated in positive-ion mode with a FAIMS Pro Interface. The LC system, configured in a vented format consisted of a fused-silica nanospray needle (PicoTip emitter, 50 µm inner diameter × 20 cm, New Objective) packed in-house with Magic C18-AQ, 5 µm and a trap (IntegraFrit Capillary, 100 µm inner diameter × 2 cm, New Objective) containing the same resin as in the analytical column with mobile phases of 0.1% formic acid in water (A) and 0.1% formic acid in acetonitrile (B). The peptide sample was diluted in 20 µl of 0.1% formic acid, 2% acetonitrile and 8.5 µl was loaded onto the column and separated over 150 min at a flow rate of 300 nL min⁻¹ with a gradient from 4 to 9% B for 2 min; 9 to 25% B for 80 min; 25 to 44% B for 60 min; 44 to 63% B for 8 min; hold 63% B for 1 min; 63 to 90% B for 11 min; and hold 90% B for 1 min. A spray voltage of 2,300 V was applied to the nanospray tip. FAIMS MS/MS analysis occurred over a 3 s cycle time consisting of 1 full scan MS from 400–1,600 m/z at a resolution of 120,000 followed by data-dependent MS/MS scans cycling through FAIMS CV of -40, -60 and -80 using HCD activation at a resolution of 50,000 with 38% normalized collision energy of the most abundant ions. Selected ions were dynamically excluded for 60 s after a repeat count of 1.

Shotgun MS data analysis. Raw MS/MS spectra from the analysis were searched against reviewed Human Universal Protein Resource (UniProt) sequence database release 2021_06 with common laboratory contaminants using MaxQuant/Andromeda⁵³ v.1.6.17.0. The search was performed with tryptic enzyme constraint set for up to two missed cleavages, oxidized methionine and phosphorylated serine, threonine and tyrosine set as a variable modification, and carbamidomethylated cysteine set as a static modification. Peptide MH⁺ mass tolerances were set at 20 ppm. The overall false-discovery rate (FDR) was set at ≤0.25% using a reverse database target decoy approach. Phosphopeptide site localization was determined by MaxQuant and converted to phosphorylation sites and reverse hits and potential contaminants were excluded from further analysis using Perseus (v.1.6.1.1)⁵⁴. Phosphosite instances were uniquely identified by leading proteins, phosphorylation site and multiplicity. The phosphosite instances with localization probability of less than or equal to 0.75 were filtered out. Phosphosite and protein intensity results were normalized by scaling each TMT channel to the channel median and then log₂ transformed.

Quantitative proteomics data were further processed with LIMMA package (v.3.52.2)⁵⁵ via R (v.4.1.3)⁵⁶. Pairwise comparisons were performed among experimental conditions. A standard linear model fitting and an empirical Bayes procedure were performed to correct the distribution. A moderated t-statistic using a simple Bayesian model was applied as the fundamental statistic, followed by multiple-testing correction using the Benjamini–Hochberg method, which is referred to as the FDR. All of these procedures were performed with limma using

the default configuration. The volcano plots were created using the *ggplot2*⁵⁷ and *ggrepel*⁵⁸ packages and were used to visualize significantly different proteins and phosphosites. Gene Ontology enrichment analysis was performed with Cellular Component subontology using the clusterProfiler Bioconductor package (v.4.6.2)⁵⁹. The LC–MS/MS proteomics data have been deposited to the ProteomeXchange Consortium⁶⁰ via the PRIDE⁶¹ partner repository with the dataset identifier PXD038386.

Analysis of mRNA Expression of TCGA tumours. For the analysis of RNA-seq mRNA expression of the Cancer Genome Atlas (TCGA) tumour versus matched normal tissues, the raw HTSeq mRNA expression counts of all TCGA samples were downloaded from the NCI Genomic Data Commons Data Portal (<https://portal.gdc.cancer.gov/>) using a custom Python script. The raw counts were normalized as counts per million (CPM) with weighted trimmed mean of *M*-values and log₂ transformed using the edgeR package⁶². Tumour and matched normal tissues were identified with sample type code of 1 and 11, respectively. The *ggpubr* R package was used to perform the two-sided Student's *t*-tests to show the difference in *CDK5* mRNA expression levels (log₂[CPM]) between the tumour and the matched normal tissue groups for each cancer type. The test results and the log₂[CPM] data were plotted using the *ggplot2* v.3.5.1 package in R.

CDK5-p35 and CDK5-cyclin B1 complex kinase activity assay. Human *CDK5* was cloned into the BamHI/NotI sites of the expression vector pFastBac. Human *CDK5* was expressed in SF9 insect cells of the Bac-to-Bac Expression System (Thermo Fisher Scientific, 10359016) according to the manufacturer's instructions. SF9 cells expressing *CDK5* were lysed with ice-cold lysis buffer (50 mM Tris pH 8.0, 150 mM NaCl, 1% NP-40 and 1 mM PMSF).

p35 and cyclin B1 were cloned into BamHI/EcoRI and BamHI/XhoI, respectively, of pTAT-HA⁶³. Then, 100 ng of pTAT-HA containing p35 or cyclin B1 was transformed into *Escherichia coli* BL21 (DE3) (Stratagene, 200131). A single colony was selected and grown at 37 °C overnight. The overnight culture was then transferred into a 1 l Erlenmeyer flask containing 600 ml of LB broth. The culture was grown for approximately 4 h until the optical density at 600 nm (OD₆₀₀) reached 0.5, at which point protein expression was induced with the addition of 100 μM of Isopropyl β-D-1-thiogalactopyranoside at 24 °C for 12 h. Cells were then collected by centrifuging at 7,000*g* for 10 min. All cell pellets were frozen at -20 °C until lysis.

Pellets were resuspended and homogenized in 10 ml of iced-cold lysis buffer (50 mM Tris pH 8.0, 500 mM NaCl, 1% NP-40, 5% glycerol and 1 mM PMSF) by vortexing three times for 1 min followed by 5 min of incubation on ice for a total duration of 15 min. Resuspended cells were further lysed with a French press (Thermo Electron) followed by centrifuging at 10,000*g* for 30 min. The soluble fraction of each recombinant protein was saved as the lysate.

Insect cell lysate of human *CDK5* was mixed at a 1:1 ratio with lysis buffer or bacterial cell lysate of p35 or cyclin B1 to form CDK5 monomer, CDK5-p35 and CDK5-cyclin B complex, respectively. Then, 10 μl of protein G beads (Sigma-Aldrich, P-3296) and 1 μl of CDK5 antibody (Santa Cruz, SC-6247) as the limiting reagent were added to the lysate mixture for immunoprecipitation of CDK5 at 4 °C for 2 h with end-over-end rotation. The beads were subsequently washed four times with PBS. The kinase reaction commenced with the addition 50 ng of a CDK5-specific peptide substrate (KHHKSPKHA), kinase assay buffer (25 mM Tris pH 8.0 and 5 mM MgCl₂) and 50 μM ATP, and proceeded at 25 °C for 30 min with gentle shaking at 800 rpm. The beads were centrifuged at 10,000*g*. The supernatant containing the reaction mixtures was mixed with reagents from the Promega Kinase-Glo Plus Luminescent Kinase Assay System (Thermo Fisher Scientific, PRV3774) according to the manufacturer's instructions to measure the relative activity.

CDK5(WT)-cyclin B1 and CDK5(S46D)-cyclin B1 complex kinase activity assay. 6×His-tagged CDK5(WT) and CDK5(S46D) were cloned into the BamHI/Ncol sites of the pTAT-HA vector. Cyclin B1 was cloned into the BamHI/XhoI sites of the pTAT-HA vector. All proteins were expressed in *E. coli* BL21 (DE3) in the same manner as described above. The lysates from these bacterial cells were prepared as described above. Preclarified lysate was pre-equilibrated with ProBond Nickel-Chelating Resin (Invitrogen life Technologies, R80101) by end-over-end rotation at 4 °C for 45 min. After flowthrough, the protein-bound resins were washed twice with low stringent buffer (50 mM Tris pH 8.0 and 150 mM NaCl), twice with medium stringent buffer (50 mM Tris pH 8.0, 150 mM NaCl and 10 mM imidazole), once with high stringent buffer (50 mM Tris pH 8.0, 150 mM NaCl and 20 mM imidazole), followed by one final wash with low stringent buffer. All proteins were eluted using elution buffer (50 mM Tris pH 8.0, 250 mM imidazole).

Then, 50 ng of purified CDK5 WT or S46D alone, or with 50 ng of cyclin B1 was incubated for 10 min with 0.2 μg of CDK5 antibody (Santa Cruz, SC-6247), and 10 μl of prewashed protein G beads (Sigma-Aldrich, P-3296) to ensure equal amounts of CDK5(WT) and CDK5(S46D) were pulled down. The immunoprecipitated CDK5 complex on the beads was subsequently washed four times with PBS. The kinase reaction commenced with the addition of 50 ng of CDK5-specific peptide substrate (KHHKSPKHA) and 50 μM ATP in kinase reaction assay buffer (25 mM Tris pH 8.0 and 5 mM MgCl₂) and conducted as described above. The relative CDK5 kinase complex activity was measured using the Promega Kinase-Glo Plus Luminescent Kinase Assay System (PRV3774) as described above.

CDK5(WT)/CDK5(S159A) complex kinase assay. RPE-1CDK5(as) cells expressing MYC-His-tagged CDK5 WT or S159A were synchronized to prometaphase by nocodazole treatment. Mitotic cells were collected by shake-off and lysed in NETN lysis buffer as described above. For MYC immunoprecipitation, 800 μg of mitotic protein lysate was mixed with MYC antibody (ab32053) for 2 h at 4 °C with end-over-end rotation, then added to 10 μl of protein A/G beads and incubated overnight at 4 °C with end-over-end rotation. The beads were washed twice with lysis buffer, then twice in kinase reaction buffer (40 mM Tris pH 8.0, 20 mM MgCl₂ and 0.1 mg ml⁻¹ BSA). The kinase reaction was carried out in kinase reaction buffer with 100 μM CDK1/CDK5 peptide substrate (KHHKSPKHR), 10 μM ATP at 25 °C for 60 min. The relative CDK5 kinase complex activity was measured using the Promega Kinase-Glo Plus Luminescent Kinase Assay System (PRV3774) as described above.

CDK1 and CDK5(as) kinase assay. RPE-1CDK5(as) cells were synchronized to prometaphase by nocodazole treatment. Mitotic cells were collected and lysed as described above for the CDK5 WT/S159A complex assay. Then, 500 μg of mitotic protein lysate was mixed with either 10 μl of CDK1 antibody-coupled agarose (Santa Cruz, sc-54 AC) bead slurry to immunoprecipitate endogenous CDK1, or with 10 μl CDK5 antibody-coupled agarose (Santa Cruz sc-249 AC) bead slurry to immunoprecipitate CDK5(as). The lysate-antibody bead mixtures were incubated overnight with end-over-end rotation at 4 °C and proceeded as described above CDK5 WT/S159A complex assay.

Immunoblotting of the immunoprecipitated CDK5 complex formed in the kinase activity assay. After the supernatant containing the kinase reaction mixture was removed for measurement of kinase activity, the beads from immunoprecipitation were washed twice with 1× PBS. Then, 60 μl of SDS loading dye (250 mM Tris-Cl pH 6.8, 8% SDS, 0.1% bromophenol blue, 40% (v/v) glycerol, and 100 mM dithiothreitol) was added to the beads and boiled for 5 min at 95 °C to elute the complex. The eluted proteins were resolved using SDS-PAGE, immunoblotted for the indicated proteins with antibodies against CDK5 (Santa Cruz, SC-6247), p35 (Santa Cruz, SC-5180100) and cyclin B1 (Santa Cruz, SC-245). The blots were detected using a chemiluminescence imager (Syngene).

Article

CDK5–cyclin B1 complex structure prediction. Amino acid sequences for human CDK5 (UniProt: Q00535), cyclin B1 (UniProt: P14635) and CDK1 (UniProt: P06493) were retrieved from UniProtKB. Structural models of heterodimer complexes between CDK5–cyclin B1 and CDK1–cyclin B1 were predicted using web-based ColabFold based on AlphaFold2-Multimer (AF2) code hosted by Google Colab (<https://colab.research.google.com/github/sokrypton/ColabFold/blob/main/AlphaFold2.ipynb#scrollTo=G4yBrceuFb3>)⁶⁴. For each prediction, the default parameters for the run, including num recycles=3 and num models=5, were used, and the models were ranked based on iPTM score. Initially, for all proteins, full-length sequences were used as the input for the prediction. The truncated cyclin B1 protein sequence was then determined by analysing the resulting complex structures to eliminate unnecessary regions that are neither part of the dimer interface nor contributing to any intramolecular interactions. As most of the predicted models for each protein pair had excellent iPTM scores (0.9 or higher), all five models for each prediction were aligned and analysed for any significant changes in the models. All structural analyses and figures were generated using Pymol (Schrödinger). Final models for CDK5–cyclin B1 and CDK1–cyclin B1 were generated by running top rank models (from AF2 predictions) through the Protein Preparation wizard in the Schrödinger suite. All minimizations were performed with OPLS4 force field⁶⁵.

Quantification and statistical analyses. Quantification of immunoblots intensity was performed using ImageJ. Prism 10 (GraphPad Software) was used for the indicated statistical analysis and production of all graphs and plots.

Reporting summary

Further information on research design is available in the Nature Portfolio Reporting Summary linked to this article.

Data availability

All data supporting the findings of this study are available in the Article and its Supplementary Information. The LC–MS/MS proteomics data have been deposited to the ProteomeXchange Consortium⁶⁰ via the PRIDE⁶¹ partner repository under dataset identifier PXD038386. Correspondence regarding experiments and requests for materials should be addressed to the corresponding authors.

51. van den Heuvel, S. & Harlow, E. Distinct roles for cyclin-dependent kinases in cell cycle control. *Science* **262**, 2050–2054 (1993).
52. Nakatani, Y. & Ogryzko, V. Immunoaffinity purification of mammalian protein complexes. *Methods Enzymol.* **370**, 430–444 (2003).
53. Tyanova, S., Temu, T. & Cox, J. The MaxQuant computational platform for mass spectrometry-based shotgun proteomics. *Nat. Protoc.* **11**, 2301–2319 (2016).
54. Tyanova, S. et al. The Perseus computational platform for comprehensive analysis of (proteo)omics data. *Nat. Methods* **13**, 731–740 (2016).
55. Ritchie, M. E. et al. limma powers differential expression analyses for RNA-sequencing and microarray studies. *Nucleic Acids Res.* **43**, e47 (2015).
56. R Core Team. R: a language and environment for statistical computing (2021).
57. Wickham, H. ggplot2: elegant graphics for data analysis (2016).

58. Slowikowski, K. ggrepel: automatically position non-overlapping text labels with “ggplot2” (2018).
59. Wu, T. et al. clusterProfiler 4.0: a universal enrichment tool for interpreting omics data. *Innovation* **2**, 100141 (2021).
60. Deutsch, E. W. et al. The ProteomeXchange consortium in 2020: enabling ‘big data’ approaches in proteomics. *Nucleic Acids Res.* **48**, D1145–D1152 (2020).
61. Perez-Riverol, Y. et al. The PRIDE database and related tools and resources in 2019: improving support for quantification data. *Nucleic Acids Res.* **47**, D442–D450 (2019).
62. Robinson, M. D., McCarthy, D. J. & Smyth, G. K. edgeR: a Bioconductor package for differential expression analysis of digital gene expression data. *Bioinformatics* **26**, 139–140 (2010).
63. Nagahara, H. et al. Transduction of full-length TAT fusion proteins into mammalian cells: TAT-p27Kip1 induces cell migration. *Nat. Med.* **4**, 1449–1452 (1998).
64. Mirdita, M. et al. ColabFold: making protein folding accessible to all. *Nat. Methods* **19**, 679–682 (2022).
65. Lu, C. et al. OPLS4: improving force field accuracy on challenging regimes of chemical space. *J. Chem. Theory Comput.* **17**, 4291–4300 (2021).
66. Obenauer, J. C., Cantley, L. C. & Yaffe, M. B. Scansite 2.0: proteome-wide prediction of cell signaling interactions using short sequence motifs. *Nucleic Acids Res.* **31**, 3635–3641 (2003).

Acknowledgements We thank D. Pellman for comments on the manuscript; W. Michowski, S. Sharma, P. Sicinski, B. Nabet and N. Gray for the reagents; J. A. Tainer for providing access to software used for structural analysis; and S. Gerber for sharing unpublished results. D.C. is supported by grants R01 CA208244 and R01 CA264900, DOD Ovarian Cancer Award W81XWH-15-0564/OC140632, Tina’s Wish Foundation, Detect Me If You Can, a V Foundation Award, a Gray Foundation grant and the Claudia Adams Barr Program in Innovative Basic Cancer Research. A. Spektor would like to acknowledge support from K08 CA208008, the Burroughs Wellcome Fund Career Award for Medical Scientists, Saverin Breast Cancer Research Fund and the Claudia Adams Barr Program in Innovative Basic Cancer Research. X.-F.Z. was an American Cancer Society Fellow and is supported by the Breast and Gynecologic Cancer Innovation Award from Susan F. Smith Center for Women’s Cancers at Dana-Farber Cancer Institute. A. Syed is supported by the Claudia Adams Barr Program in Innovative Basic Cancer Research. B.T. was supported by the Polish National Agency for Academic Exchange (grant PPN/WAL/2019/1/00018) and by the Foundation for Polish Science (START Program). A.D.D is supported by NIH grant R01 HL52725. A.G.P. by National Cancer Institute grants U01CA214114 and U01CA217407, as well as a donation from the Aven Foundation; J.R.W. by National Cancer Institute grant R50CA211499; and K.S. by NIH awards 1R01-CA237660 and 1RF1NS124779.

Author contributions X.-F.Z., A. Sarkar, A. Spektor, and D.C. conceived the project and designed the experiments. X.-F.Z. and A. Sarkar performed the majority of experiments and associated analyses except as listed below. H.L. expressed relevant proteins and conducted the kinase activity assays for CDK5–cyclin B1, CDK5–p35 and CDK5(S46) variant complexes under the guidance of K.S.; A. Syed performed structural modelling and analysis. R.G.I., J.J.K. and J.R.W. performed MS and analysis. B.T. and H.N. performed MS data analyses. K.H. provided guidance to screen CDK5(as) knocked-in clones and performed sequence analysis to confirm CDK5(as) knock-in. F.L. and A.D.D. provided reagents and discussion on CDK5 substrates analyses. X.-F.Z., A. Sarkar, A. Spektor and D.C. wrote the manuscript with inputs and edits from all of the other authors.

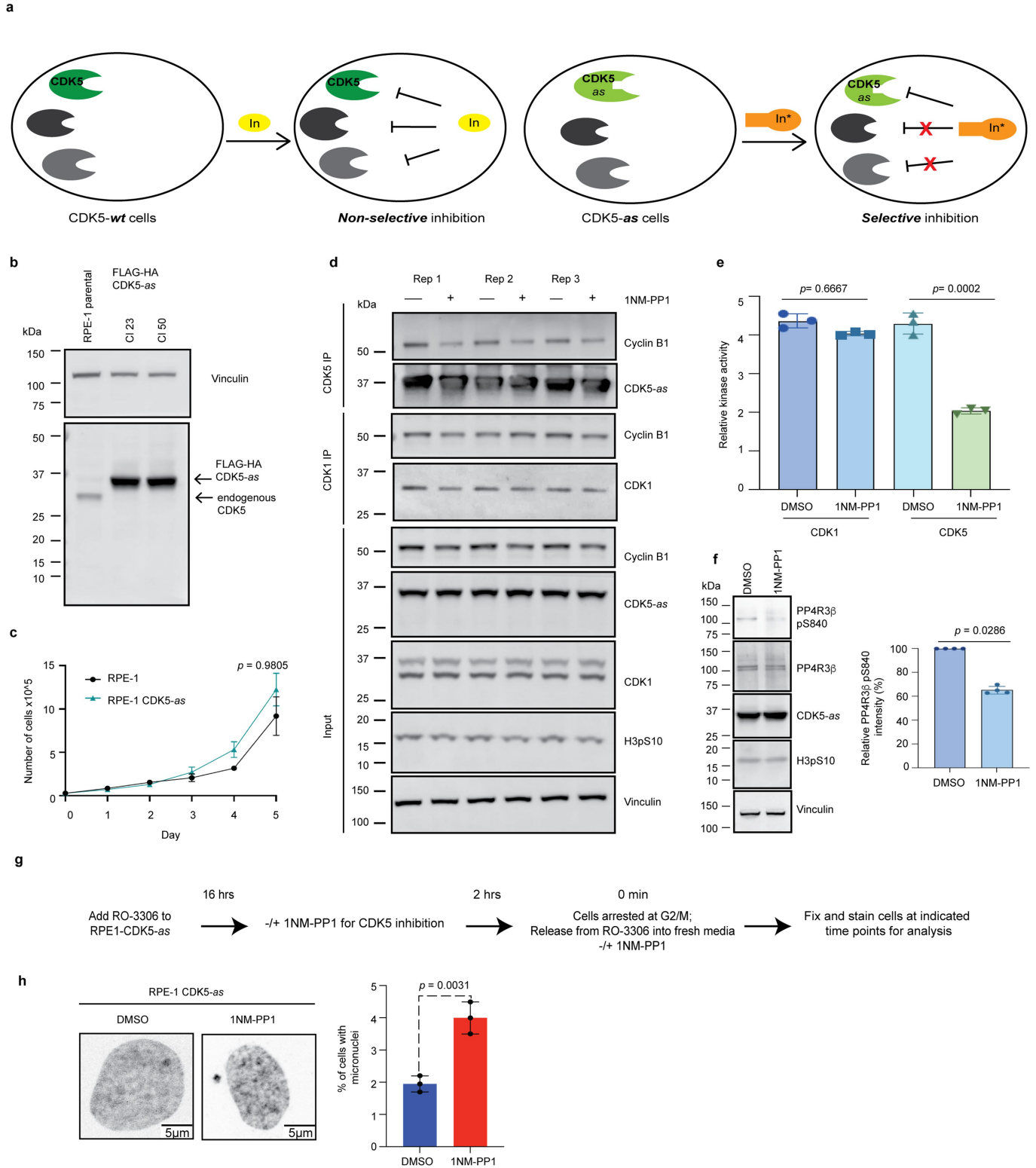
Competing interests A.D.D. reports consulting for AstraZeneca, Bayer AG, Blacksmith/Lightstone Ventures, Bristol Myers Squibb, Cyteir Therapeutics, EMD Serono, Impact Therapeutics, PrimeFour Therapeutics, Pfizer, Tango Therapeutics and Zentalis Pharmaceuticals/Zeno Management; is an advisory board member for Cyteir and Impact Therapeutics; a stockholder in Cedilla Therapeutics, Cyteir, Impact Therapeutics and PrimeFour Therapeutics; and reports receiving commercial research grants from Bristol Myers Squibb, EMD Serono, Moderna and Tango Therapeutics. The other authors declare no competing interests.

Additional information

Supplementary information The online version contains supplementary material available at <https://doi.org/10.1038/s41586-024-07888-x>.

Correspondence and requests for materials should be addressed to Alexander Spektor or Dipanjan Chowdhury.

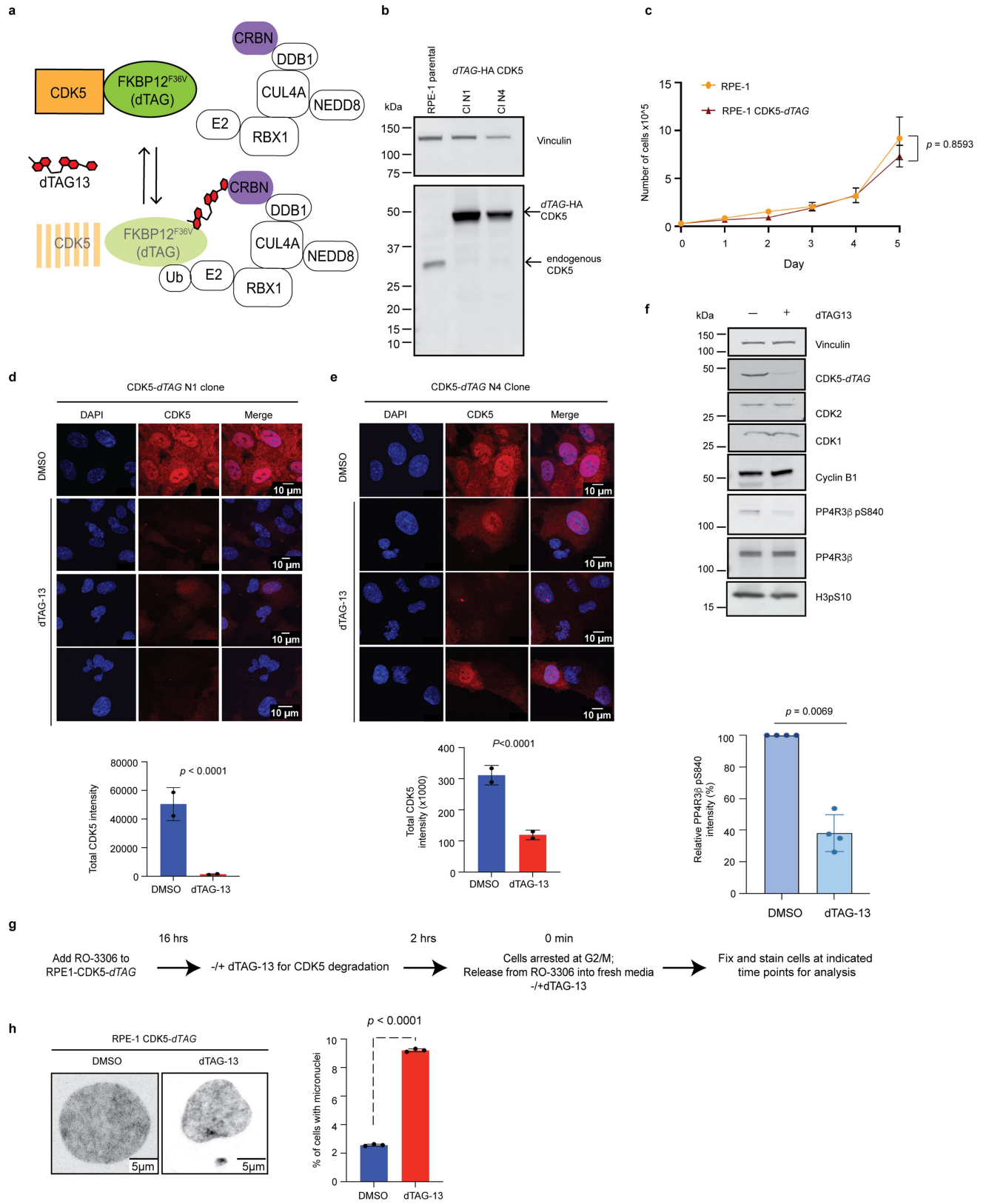
Peer review information *Nature* thanks Yibing Shan and the other, anonymous, reviewer(s) for their contribution to the peer review of this work. Peer reviewer reports are available. Reprints and permissions information is available at <http://www.nature.com/reprints>.



Extended Data Fig. 1 | See next page for caption.

Article

Extended Data Fig. 1 | Inhibition of CDK5 in analogue-sensitive (CDK5-as) system. **a**, Schematics depicting specific inhibition of the CDK5 analogue-sensitive (*as*) variant. Canonical ATP-analogue inhibitor (In, yellow) targets endogenous CDK5 (dark green) at its ATP-binding catalytic site nonspecifically since multiple kinases share structurally similar catalytic sites (left panel). The analogue-sensitive (*as*, light green) phenylalanine-to-glycine (F80G) mutation confers a structural change adjacent to the catalytic site of CDK5 that does not impact its catalysis but accommodates the specific binding of a non-hydrolysable bulky orthogonal inhibitor 1NM-PP1 (In*, orange). Introduction of 1NM-PP1 thus selectively inhibits CDK5-*as* variant (right panel). **b**, Immunoblots showing two clones (Cl 23 and Cl 50) of RPE-1 cells expressing FLAG-HA-CDK5-*as* in place of endogenous CDK5. Representative results are shown from three independent repeats. **c**, Proliferation curve of parental RPE-1 and RPE-1 CDK5-*as* cells. Data represent mean \pm s.d. from three independent repeats. *p*-value was determined by Mann Whitney U test. **d**, Immunoblots showing immunoprecipitated CDK1-cyclin B1 complex or CDK5-*as*-cyclin B1 complex by the indicated antibody-coupled agarose, from nocodazole arrested RPE-1 CDK5-*as* cells with or without 1NM-PP1 for inhibition of CDK5-*as*, from three independent replicate experiments. **e**, *In-vitro* kinase activity quantification of immunoprecipitated complex shown in **d**. Data represent mean \pm s.d. from three independent experiments. *p*-values were determined by unpaired, two-tailed student's t-test. **f**, Immunoblots of RPE-1 CDK5-*as* cells treated with either DMSO or 1NM-PP1 for 2 h prior to and upon release from RO-3306 and collected at 60 min following release. Cells were lysed and blotted with anti-bodies against indicated proteins (upper panel). Quantification of the relative intensity of PP4R3 β phosphorylation at S840 in 1NM-PP1-treated CDK5-*as* cells compared to DMSO-treatment (lower panel). **g**, Experimental scheme for specific and temporal abrogation of CDK5 in RPE-1 CDK5-*as* cells. Data represent mean \pm S.D from quadruplicate repeats. *p*-value was determined by one sample t and Wilcoxon test. **h**, Hoechst staining showing primary nuclei and micronuclei of RPE-1 CDK5-*as* with indicated treatment; scale bar is as indicated (left panel). Right, quantification of the percentage of cells with micronuclei after treatment. Data represent mean \pm s.d. of three independent experiments from n = 2174 DMSO, n = 1788 1NM-PP1 where n is the number of cells. *p*-values were determined by unpaired, two-tailed student's t-test. Scale bar is as indicated. Uncropped gel images are provided in Supplementary Fig. 1.



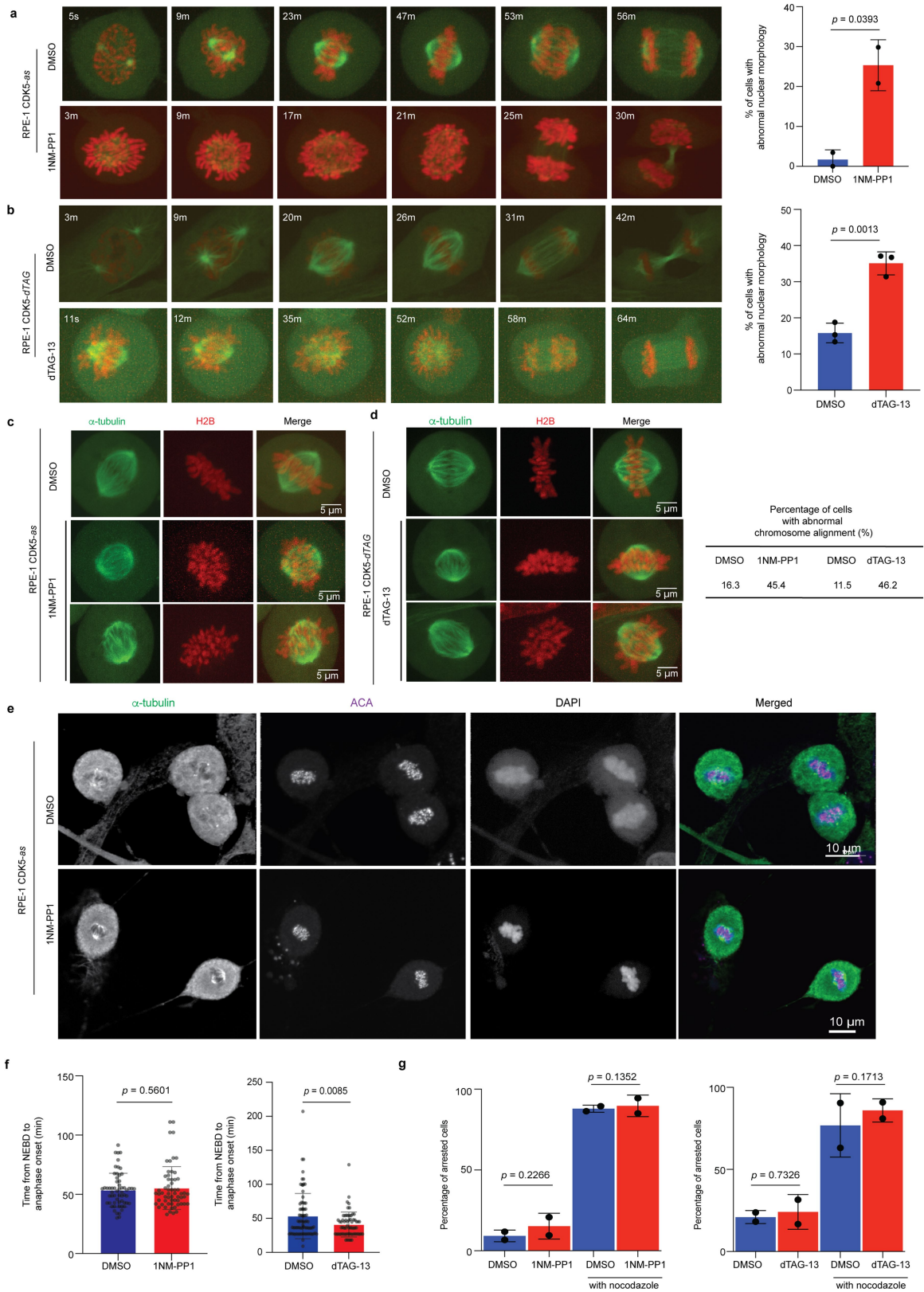
Extended Data Fig. 2 | See next page for caption.

Article

Extended Data Fig. 2 | Degradation of CDK5 in degradation tag (CDK5-dTAG) system.

a, Schematic depicting the dTAG-13-inducible protein degradation system. Compound dTAG-13 links protein fused with FKBP12^{F36V} domain (dTAG) to CRBN-DDB1-CUL4A E3 ligase complex, leading to CRBN-mediated degradation. **b**, Immunoblots showing two clones of RPE-1 cells that express *dTAG-HA-CDK5* in place of endogenous CDK5 (Cl N1 and Cl N4). Representative results are shown from three independent repeats. **c**, Proliferation curve of parental RPE-1 and RPE-1CDK5-dTAG. Data represent mean \pm s.d. of three independent repeats. *p*-value was determined by Mann Whitney U test. **d** and **e**, Representative images of RPE-1CDK5-dTAG clone 1 (N1) (**d**) and RPE-1CDK5-dTAG clone 4 (N4) (**e**) treated with DMSO or dTAG-13 for 2 h prior to and upon release from G2/M arrest and fixed at 120 min after release (top panel); quantification of CDK5 total intensity per cell (lower panels). Data represent mean \pm s.d. of at least two independent experiments from $n = 100$ cells each condition. *p*-values were determined by unpaired, two-tailed

student's t-test. **f**, Immunoblots showing level of indicated proteins in RPE-1 CDK5-dTAG cells. Cells were treated with either DMSO or dTAG-13 for 2 h prior to and upon release from RO-3306 and lysed at 60 min following release (upper panel). Quantification of the relative intensity of PP4R3 β phosphorylation at S840 in dTAG13-treated CDK5-dTAG cells compared to DMSO-treatment (lower panel). Data represent mean \pm s.d. of four independent experiments. *p*-value was determined by one sample t and Wilcoxon test. **g**, Experimental scheme for specific and temporal abrogation of CDK5 in RPE-1CDK5-dTAG cells. **h**, Hoechst staining showing primary nuclei and micronuclei of RPE-1CDK5-dTAG with indicated treatment; scale bar is as indicated (left panel). Right, quantification of the percentage of cells with micronuclei after treatment. Data represent mean \pm s.d. of three independent experiments from $n = 2094$ DMSO and $n = 2095$ dTAG-13, where n is the number of cells. *p*-values were determined by unpaired, two-tailed student's t-test. Scale bar is as indicated. Uncropped gel images are provided in Supplementary Fig. 1.

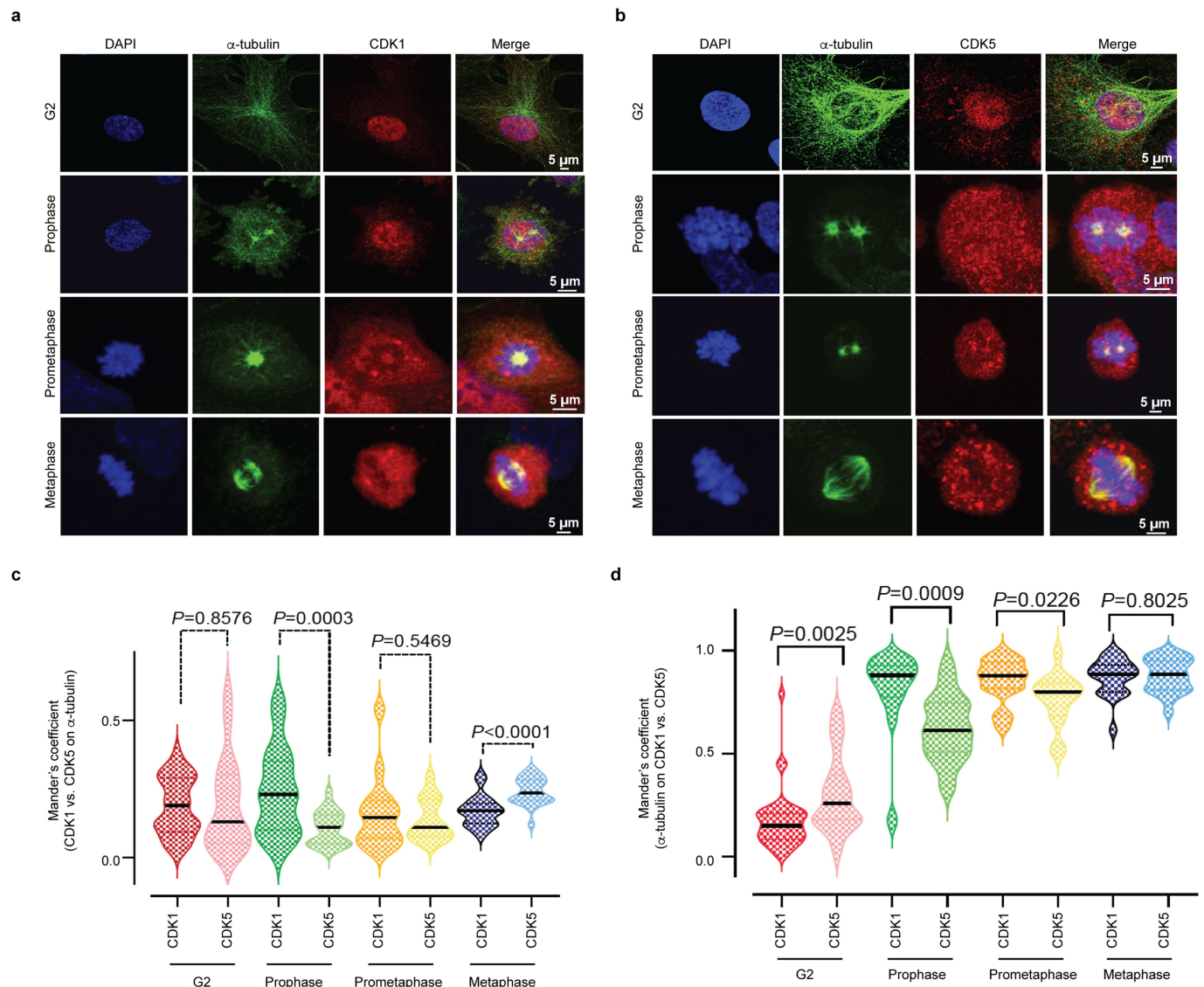


Extended Data Fig. 3 | See next page for caption.

Article

Extended Data Fig. 3 | CDK5 abrogation render chromosome alignment and segregation defect despite intact spindle assembly checkpoint and timely mitotic duration. **a** and **b**, Live-cell imaging snapshots of RPE-1 CDK5-*as* cells (**a**) and RPE-1 CDK5-*dTAG* cells (**b**) expressing mCherry-H2B and GFP- α -tubulin, abrogated of CDK5 by treatment with 1NM-PP1 or dTAG-13, respectively. Imaging commenced in prophase following release from RO-3306 into fresh media containing indicated chemicals (left); quantification of the percentage of cells with abnormal nuclear morphology (right). **c** and **d**, Representative snapshots of the final frame prior to metaphase-to-anaphase transition from a live-cell imaging experiment detailing chromosome alignment at the metaphase plate of RPE- CDK5-*as* (**c**) and RPE-1 CDK5-*dTAG* (**d**) expressing mCherry-H2B, and GFP- α -tubulin (left); quantification of the percentage of cells displaying abnormal chromosome alignment following indicated treatments (top right). **e**, Representative images showing the range of depolymerization outcomes (low polymers, high polymers and spindle-like) in DMSO- and 1NM-PP1-treated cells, as shown in Fig. 2e, from n = 50 for each condition, where n is number of metaphase cells. **f**, Quantifications of mitotic

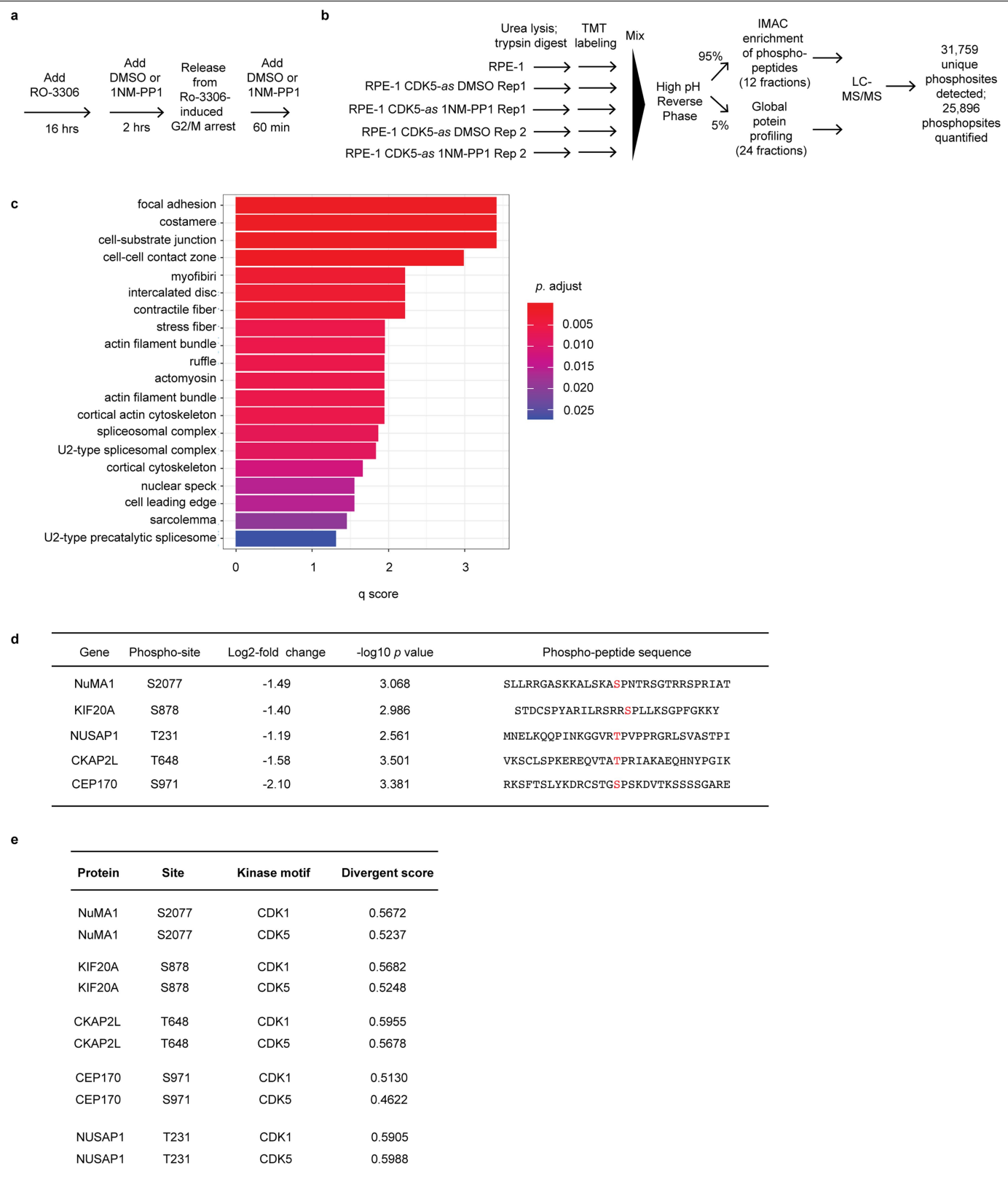
duration from nuclear envelope breakdown (NEBD) to anaphase onset of RPE-1 CDK5-*as* (left) and RPE-1 CDK5-*dTAG* (right) cells, following the indicated treatments. Live-cell imaging of RPE-1 CDK5-*as* and RPE-1 CDK5-*dTAG* cells expressing mCherry-H2B and GFP-BAF commenced following release from RO-3306 arrest into fresh media containing DMSO or 1NM-PP1 or dTAG-13. **g**, Quantifications of the percentage of RPE-1 CDK5-*as* (left) and RPE-1 CDK5-*dTAG* (right) cells that were arrested in mitosis following the indicated treatments. Imaging commenced in prophase cells as described in **a**, following release from RO-3306 into fresh media in the presence or absence nocodazole as indicated. The data in **a**, **c**, and **g** represent mean \pm s.d. of at least two independent experiments from n = 85 DMSO and n = 78 1NM-PP1 in **a** and **c**; from n = 40 cells for each treatment condition in **g**. The data in **b**, **d**, and **f** represent mean \pm s.d. of three independent experiments from n = 57 DMSO and n = 64 dTAG-13 in **b** and **d**; from n = 78 DMSO and n = 64 1NM-PP1; n = 59 DMSO and n = 60 dTAG-13, in **f**, where n is the number of cells. p-values were determined by unpaired, two-tailed student's t-test. Scale bar is as indicated.



Extended Data Fig. 4 | CDK5 and CDK1 regulate tubulin dynamics.
a, b. Immunostaining of RPE-1 cells with antibodies against CDK1 and α -tubulin (**a**); and CDK5 and α -tubulin (**b**) at indicated stages of mitosis. **c, d.** Manders' overlap coefficient M1 (CDK1 versus CDK5 on α -tubulin) (**c**); and M2 (α -tubulin

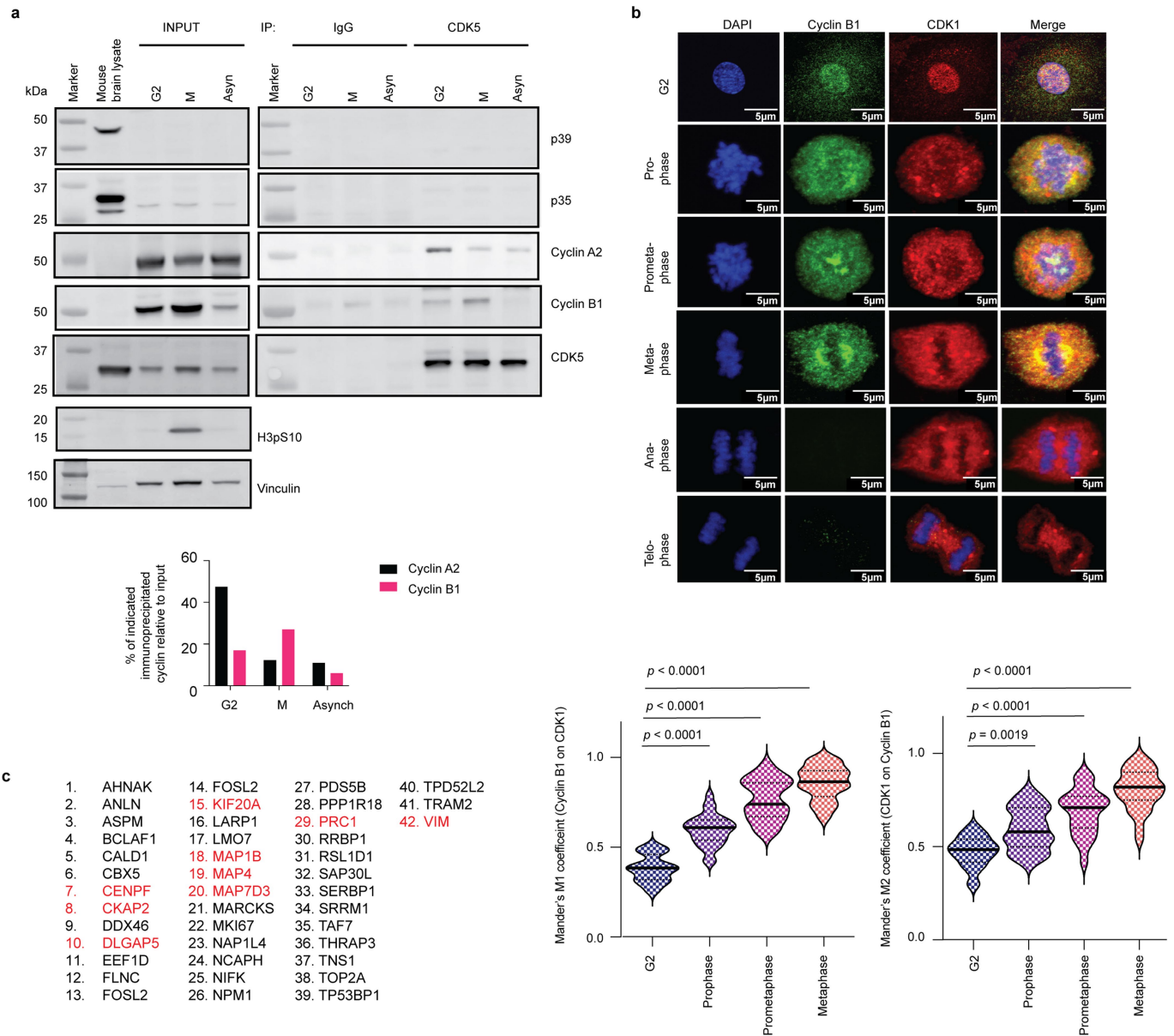
on CDK1 versus CDK5) (**d**) at indicated phases of mitosis in cells shown in **a** and **b**. The data represent mean \pm s.d. of at least two independent experiments from $n = 25$ cells in each mitotic stage. p -values were determined by unpaired, two-tailed student's t-test.

Article



Extended Data Fig. 5 | Phosphoproteomics analysis to identify mitotic CDK5 substrates. **a**, Scheme of cell synchronization for phosphoproteomics: RPE-1 CDK5-as cells were arrested at G2/M by treatment with RO-3306 for 16 h. The cells were treated with 1NM-PP1 to initiate CDK5 inhibition. 2 h post-treatment, cells were released from G2/M arrest into fresh media with or without 1NM-PP1 to proceed through mitosis with or without continuing inhibition of CDK5. Cells were collected at 60 min post-release from RO-3306 for lysis. **b**, Schematic for phosphoproteomics-based identification of putative

CDK5 substrates. **c**, Gene ontology analysis of proteins harbouring CDK5 inhibition-induced up-regulated phosphosites. **d**, Table indicating phospho-site of proteins that are down-regulated as result of CDK5 inhibition. **e**, Table indicating the likely kinases to phosphorylate the indicated phosphosites of the protein, as predicted by Scansite 4⁶⁶. Divergent score denotes the extent by which phosphosite diverge from known kinase substrate recognition motif, hence higher divergent score indicating the corresponding kinase is less likely to phosphorylate the phosphosite.



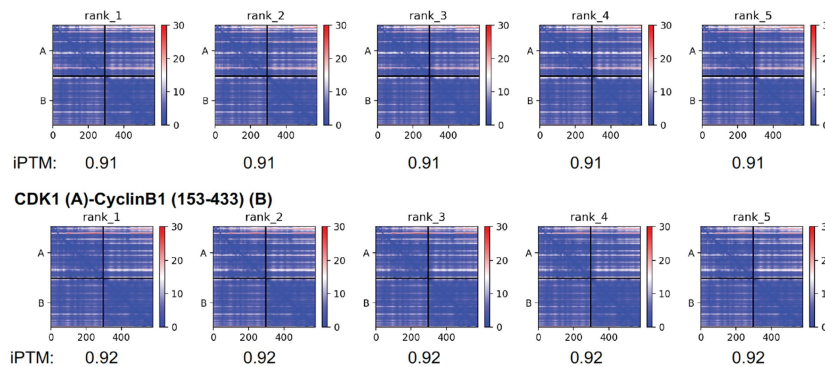
Extended Data Fig. 6 | Cyclin B1 is a mitotic co-factor of CDK5 and of CDK1.
a, Endogenous CDK5 was immunoprecipitated from RPE-1 cells collected at time points corresponding to the indicated cell cycle stage. Cell lysate input and elution of immunoprecipitation were immunoblotted by antibodies against the indicated proteins. RPE-1 cells were synchronized to G2 by RO-3306 treatment for 16 h and to prometaphase (M) by nocodazole treatment for 6 h. Asynch: Asynchronous. Uncropped gel images are provided in Supplementary Fig. 1. **b**, Immunostaining of RPE-1 cells with antibodies against the indicated proteins at indicated mitotic stages (upper panels). Manders' overlap coefficient M1 (Cyclin B1 on CDK1) and M2 (CDK1 on Cyclin B1) at indicated

mitotic stages for in cells shown in **b** (lower panels). The data represent mean \pm s.d. of at least two independent experiments from $n = 25$ mitotic cells in each mitotic stage. p -values were determined by unpaired, two-tailed student's t-test. **c**, Table listing common proteins as putative targets of CDK5, uncovered from the phosphoproteomics analysis of down-regulated phosphoproteins upon CDK5 inhibition (Fig. 3 and Supplementary Table 1), and those of cyclin B1, uncovered from phosphoproteomics analysis of down-regulated phosphoproteins upon cyclin B1 degradation (Fig. 6 and Table EV2 in Hegar et al. EMBOJ. 2020). Proteins relevant to mitotic functions are highlighted in red.

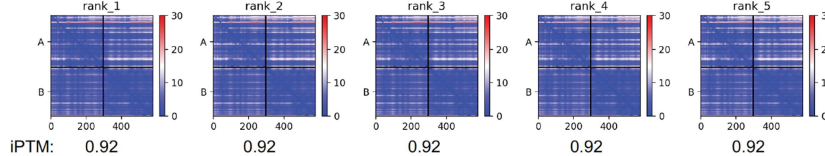
Article

a

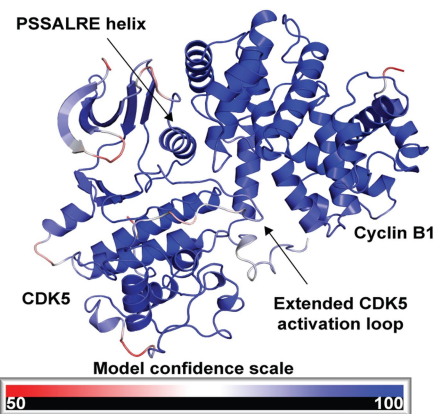
CDK5 (A)-CyclinB1 (153-433) (B)



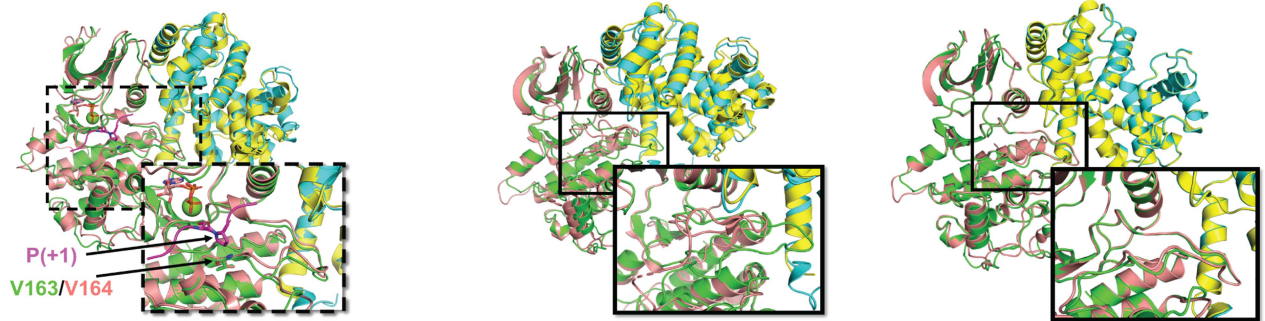
CDK1 (A)-CyclinB1 (153-433) (B)



b



c

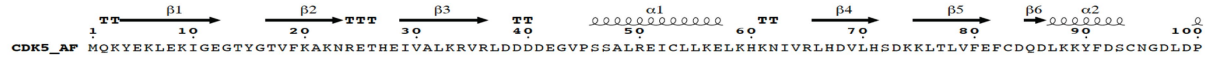


CDK5-Cyclin B1 / pCDK2-Cyclin A3-Substrate

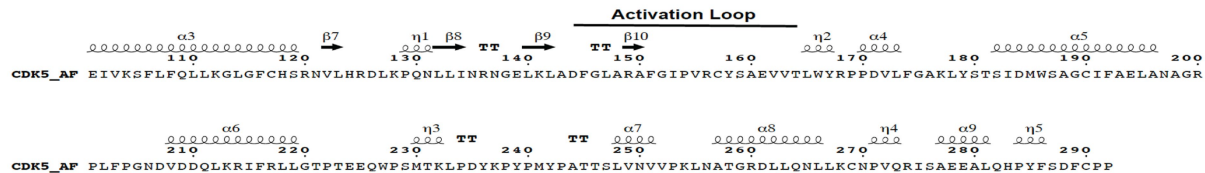
CDK5-Cyclin B1 / CDK1-Cyclin B1

CDK5-Cyclin B1 / CDK1-Cyclin B1

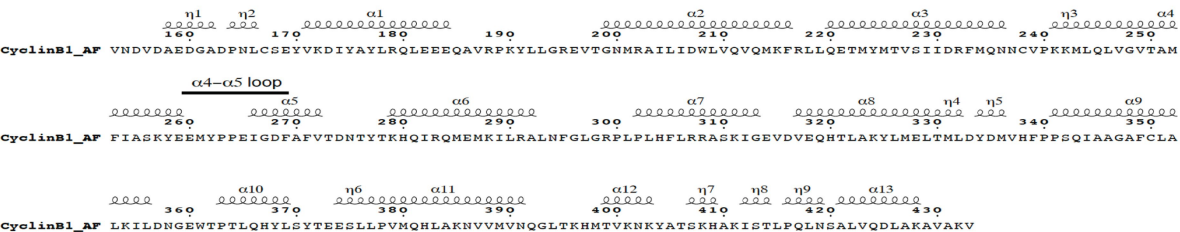
d



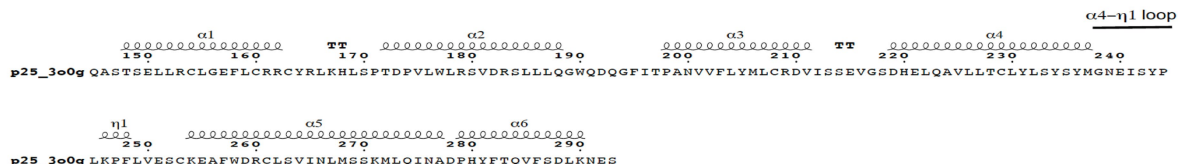
i



ii



iii

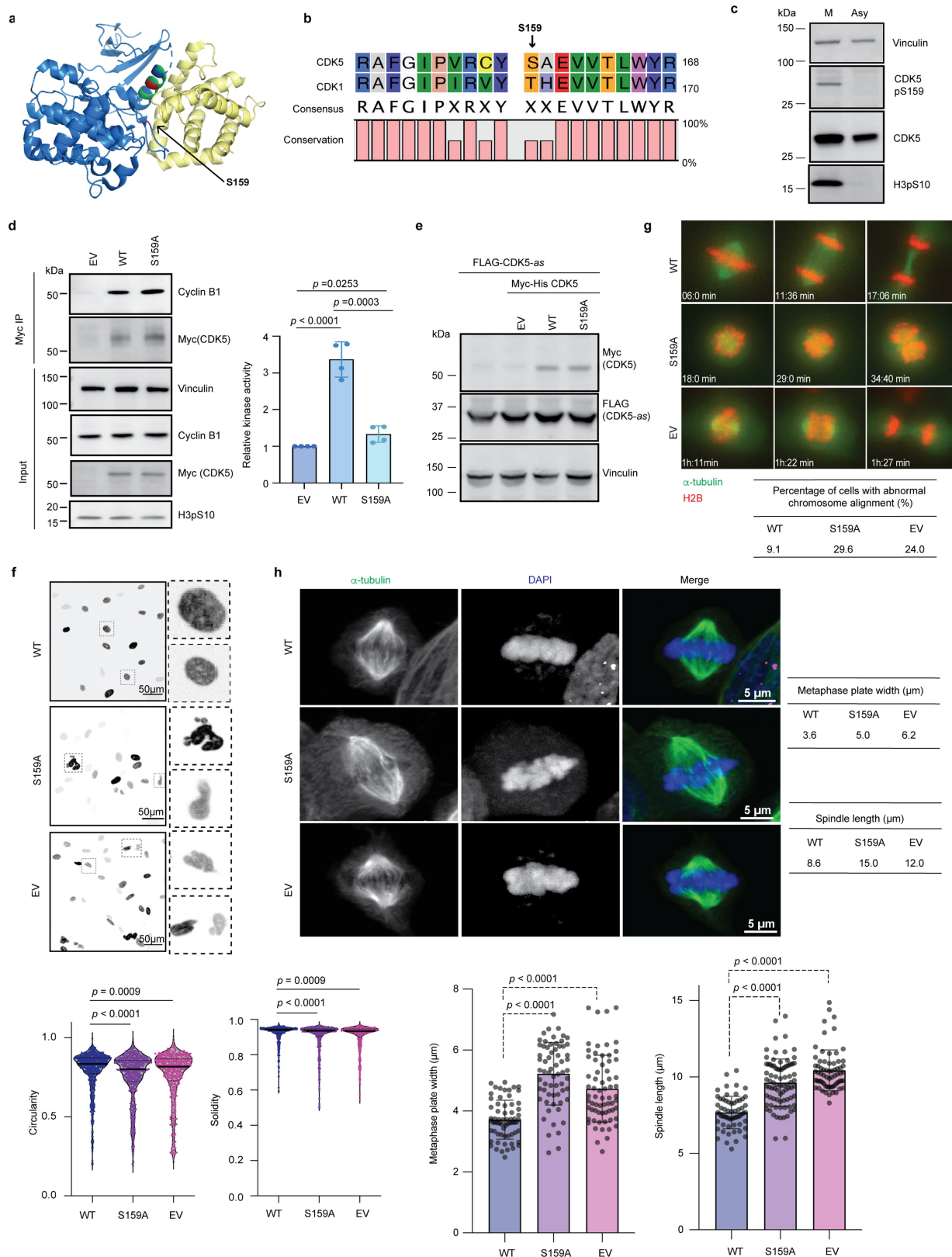


Extended Data Fig. 7 | See next page for caption.

Extended Data Fig. 7 | Structural prediction and analyses of the CDK5-cyclin B1 complex. **a**, Predicted alignment error (PAE) plots of the top five AlphaFold2 (AF2)-predicted models of CDK5-cyclin B1 (top row) and CDK1-cyclin B1 (bottom row) complexes, ranked by interface-predicted template (iPTM) scores. **b**, AlphaFold2-Multimer-predicted structure of the CDK5-cyclin B1 complex. **c**, Structural comparison of CDK-cyclin complexes. Left most panel: Structural-overlay of AF2 model of CDK5-cyclin B1 and crystal structure of phospho-CDK2-cyclin A3-substrate complex (PDB ID:1QMZ). The zoomed-in view of the activation loops of CDK5 and CDK2 is shown in the inset. V163 (in CDK5), V164 (in CDK2) and Proline at +1 position in the substrates are indicated with arrows. Middle panel: Structural-overlay of AF2 model of

CDK5-cyclin B1 and crystal structure of CDK1-cyclin B1-Cks2 complex (PDB ID:4YC3). The zoomed-in view of the activation loops of CDK5 and CDK1 is shown in the inset. Cks2 has been removed from the structure for clarity. Right most panel: structural-overlay of AF2 models of CDK5-cyclin B1 and CDK1-cyclin B1 complex. The zoomed view of the activation loops of CDK5 and CDK1 is shown in the inset. **d**, Secondary structure elements of CDK5, cyclin B1 and p25. The protein sequences, labelled based on the structural models, are generated by PSPript for CDK5 (AF2 model) (**i**), cyclin B1 (AF2 model) (**ii**) and p25 (PDB ID:3OOG) (**iii**). Structural elements (α , β , η) are defined by default settings in the program. Key loops highlighted in Fig. 4d are mapped onto the corresponding sequence.

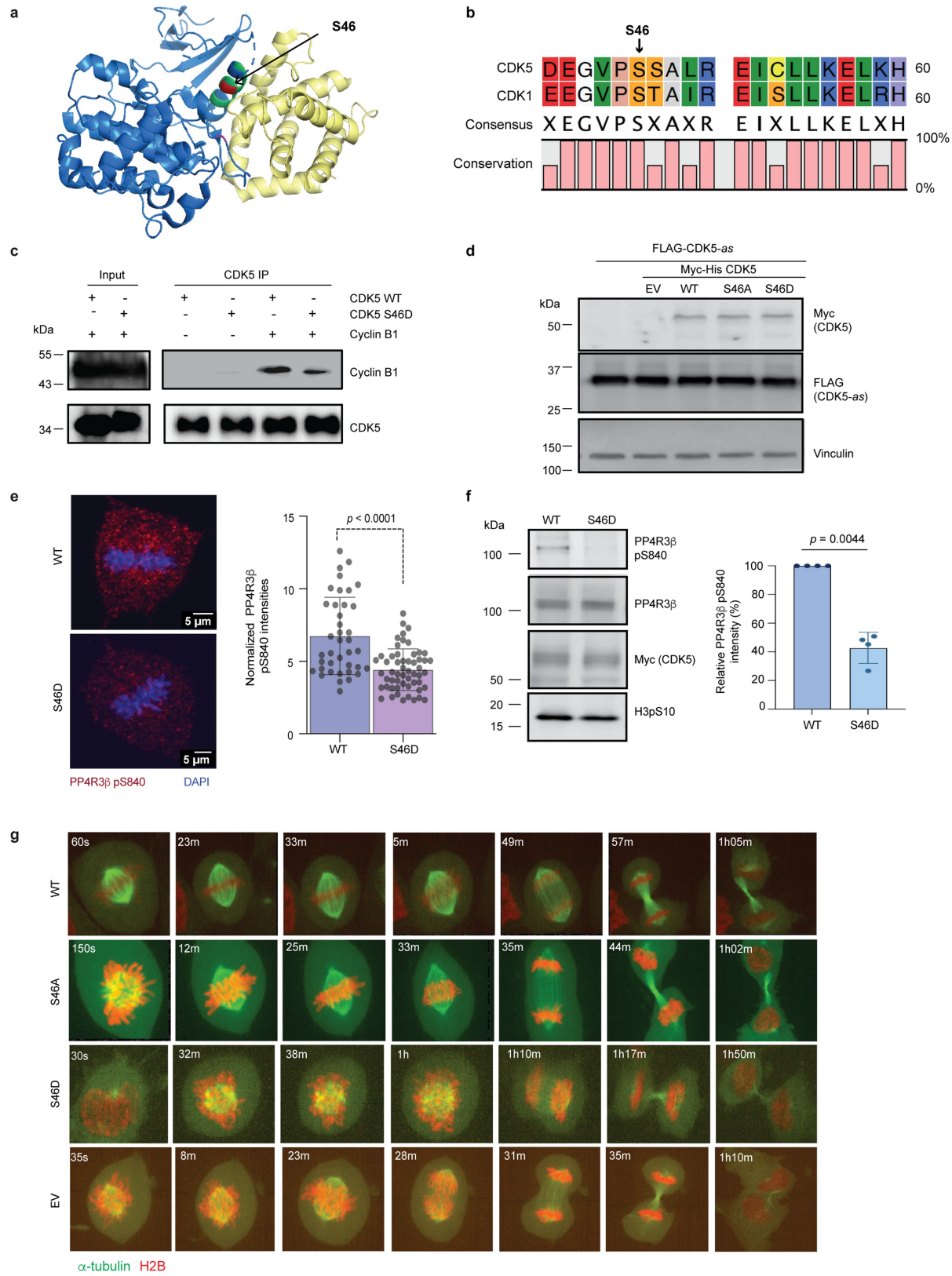
Article



Extended Data Fig. 8 | See next page for caption.

Extended Data Fig. 8 | Phosphorylation of CDK5 S159 is required for kinase activity and mitotic fidelity. **a**, Structure of the CDK5-p25 complex (PDB ID: 1h4l). CDK5 (blue) interacts with p25 (yellow). Serine159 (S159, magenta) is in the T-loop. **b**, Sequence alignment of CDK5 and CDK1 shows that S159 in CDK5 is the analogous phosphosite as that of T161 in CDK1 for T-loop activation. Sequence alignment was performed by CLC Sequence Viewer (<https://www.qiagenbioinformatics.com/products/clc-sequence-viewer/>). **c**, Immunoblots of indicated proteins in nocodazole-arrested mitotic (M) and asynchronous (Asy) HeLa cell lysate. **d**, Myc-His-tagged CDK5 S159 variants expressed in RPE-1 CDK5-*as* cells were immunoprecipitated from nocodazole-arrested mitotic lysate by Myc-agarose. Input from cell lysate and elution from immunoprecipitation were immunoblotted with antibodies against indicated protein. EV= empty vector. In vitro kinase activity assay of the indicated immunoprecipitated complex shown on the right panel. Data represent mean \pm s.d. of four independent experiments. *p*-values were determined by unpaired two-tailed student's t-test. **e**, Immunoblots showing RPE-1 FLAG-CDK5-*as* cells stably expressing Myc-His-tagged CDK5 WT and S159A, which were used in live-cell imaging and immunofluorescence experiments to characterize chromosome alignment and spindle architecture during mitosis, following inhibition of CDK5-*as* by 1NM-PP1, such that only the Myc-His-tagged CDK5 WT and S159A are not inhibited. Representative results are shown from three independent repeats. **f**, Hoechst staining showing nuclear morphology of

RPE-1 CDK5-*as* cells expressing indicated CDK5 S159 variants following treatment with either DMSO or 1NMP-PP1 and fixation at 120 min post-release from RO-3306-induced arrest (upper panel); quantification of nuclear circularity and solidity (lower panels) **g**, Snapshots of live-cell imaging RPE-1 CDK5-*as* cells expressing indicated CDK5 S159 variant, mCherry-H2B, and GFP- α -tubulin, after release from RO-3306-induced arrest at G2/M, treated with 1NM-PP1 2 h prior to and upon release from G2/M arrest (upper panel); quantification of cells displaying abnormal chromosome alignment in (lower panel). Representative images are shown from two independent experiments, $n = 30$ cells each cell line. **h**, Representative images of RPE-1 CDK5-*as* cells expressing indicated CDK5 S159 variants in metaphase, treated with DMSO or 1NM-PP1 for 2 h prior to and upon release from RO-3306-induced arrest, and then released into media containing 20 μ M proTAME for 2 h, fixed and stained with tubulin and DAPI (upper panel); metaphase plate width and spindle length measurements for these representative cells were shown in the table on right; quantification of metaphase plate width and spindle length following the indicated treatments (lower panel). Data in **f** and **h** represent mean \pm s.d. of at least two independent experiments from $n = 486$ WT, $n = 561$ S159A, and $n = 401$ EV, where n is the number of cells in **f**; from $n = 65$ WT, $n = 64$ S159A, and $n = 67$ EV, where n is the number of cells in **h**. Scale bar is as indicated. Uncropped gel images are provided in Supplementary Fig. 1.



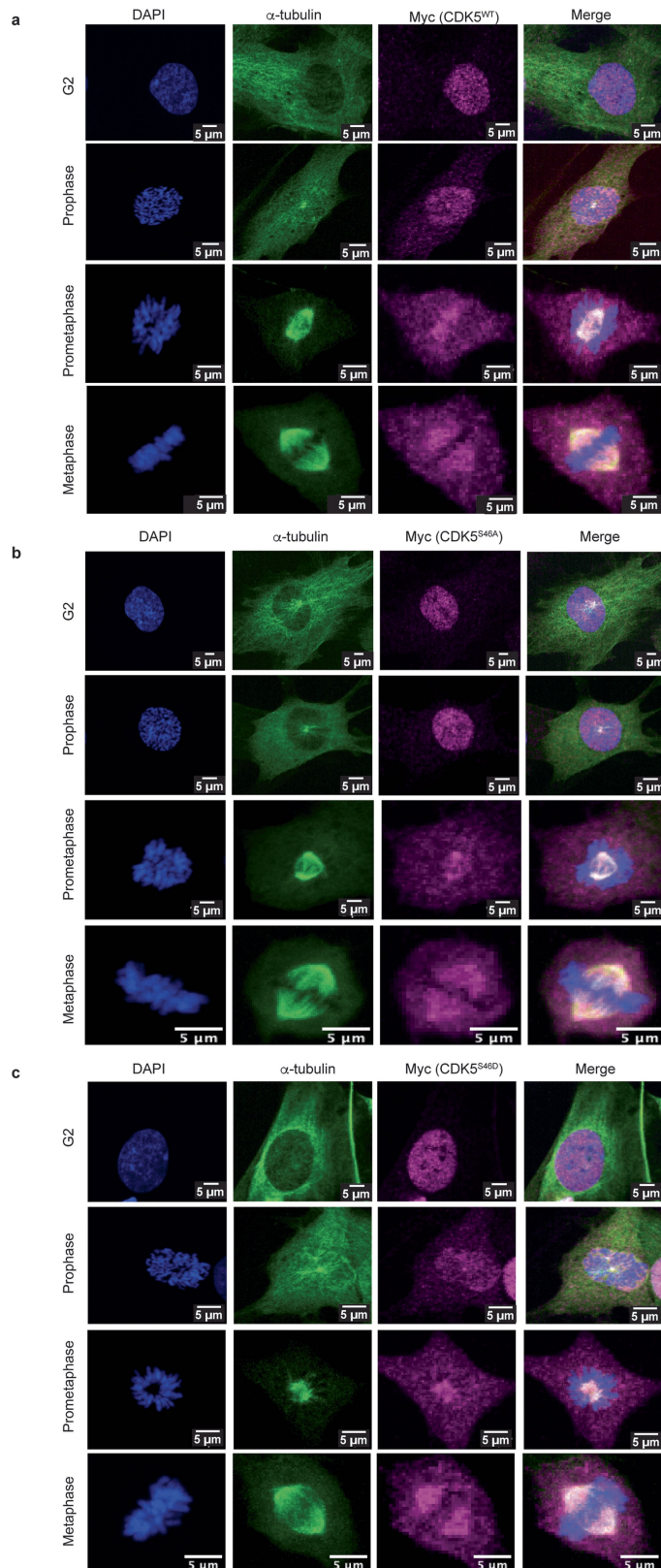
Extended Data Fig. 9 | See next page for caption.

Extended Data Fig. 9 | The CDK5 co-factor-binding helix regulates CDK5 kinase activity.

a, Structure of the CDK5-p25 complex (PDB ID: 1h41). CDK5 (blue) interacts with p25 (yellow) at the PSSALRE helix (green). Serine 46 (S46, red) is in the PSSALRE helix. Serine 159 (S159, magenta) is in the T-loop. **b**, Sequence alignment of CDK5 and CDK1 shows that S46 is conserved in CDK1 and CDK5. Sequence alignment was performed by CLC Sequence Viewer (<https://www.qiagenbioinformatics.com/products/clc-sequence-viewer/>). **c**, Immunoblots of CDK5 immunoprecipitation from lysate of *E. coli* BL21 (DE3) expressing His-tagged human CDK5 WT or CDK5 S46D, mixed with lysate of *E. coli* BL21 (DE3) expressing His-tagged human cyclin B1. Immunoprecipitated CDK5 alone or in the indicated complex were used in kinase activity assay, shown in Fig. 5b. Representative results are shown from three independent repeats. **d**, Immunoblots showing RPE-1 FLAG-CDK5-*as* cells stably expressing Myc-His-tagged CDK5 S46 phospho-variants, which were used in live-cell imaging and immunofluorescence experiments to characterize chromosome alignment and spindle architecture during mitosis, following inhibition of CDK5-*as* by INM-PP1, such that only the Myc-His-tagged CDK5 S46 phospho-variants are not inhibited. Representative results are shown from three independent repeats. **e**, Immunostaining of RPE-1 CDK5-*as* cells expressing

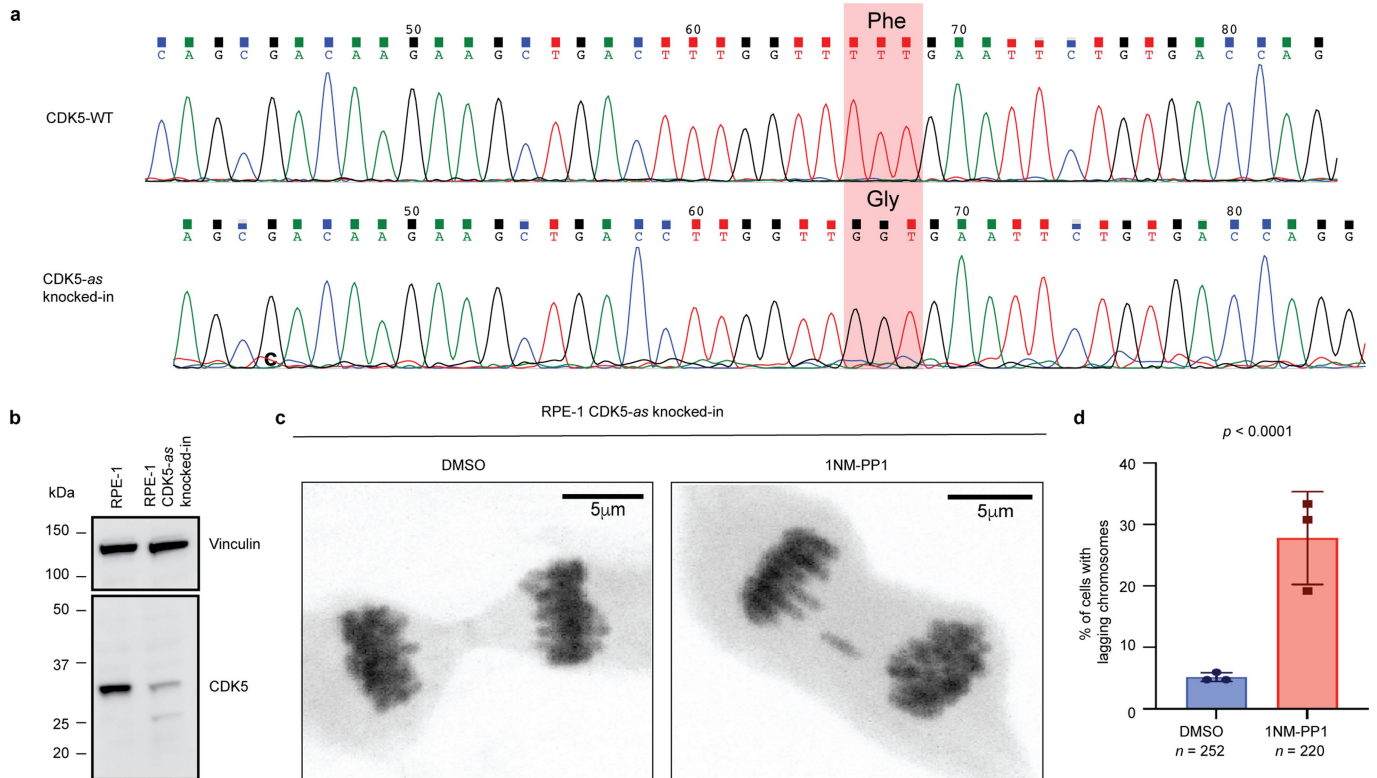
Myc-His-tagged CDK5 WT or S46D with anti-PP4R3 β S840 (pS840) antibody following indicated treatment (DMSO vs 1NM-PP1). Scale bar is as indicated (left). Normalized intensity level of PP4R3 β S840 phosphorylation (right). Data represent mean \pm s.d. of at least two independent experiments from $n = 40$ WT and $n = 55$ S46D, where n is the number of metaphase cells. p -values were determined by unpaired two-tailed student's t-test. **f**, Immunoblots showing level of indicated proteins in RPE-1 CDK5-*as* cells expressing Myc-His-tagged CDK5 WT or S46D. Cells were treated with either DMSO or 1NM-PP1 for 2 h prior to and upon release from RO-3306 and collected and lysed at 60 min following release (left). Quantification of the intensity of PP4R3 β phosphorylation at S840 (right). Data represent mean \pm s.d. of four independent experiments. p -values were determined by two-tailed one sample t and Wilcoxon test. **g**, Representative snapshots of live-cell imaging of RPE-1 CDK5-*as* cells harbouring indicated CDK5 S46 variants expressing mCherry-H2B and GFP- α -tubulin, treated with 1NM-PP1, as shown in Fig. 5d, from $n = 35$ cells. Imaging commenced in prophase following release from RO-3306 into fresh media containing indicated chemicals. Uncropped gel images are provided in Supplementary Fig. 1.

Article



Extended Data Fig. 10 | Localization of CDK5 S46 phospho-variants.

Immunostaining of RPE-1 CDK5-as cells stably expressing Myc-His CDK5-WT (a), S46A (b), and S46D (c) with antibodies against indicated protein in prophase, prometaphase, and metaphase. Data represent at least two independent experiments from $n = 25$ cells of each condition in each mitotic stage.

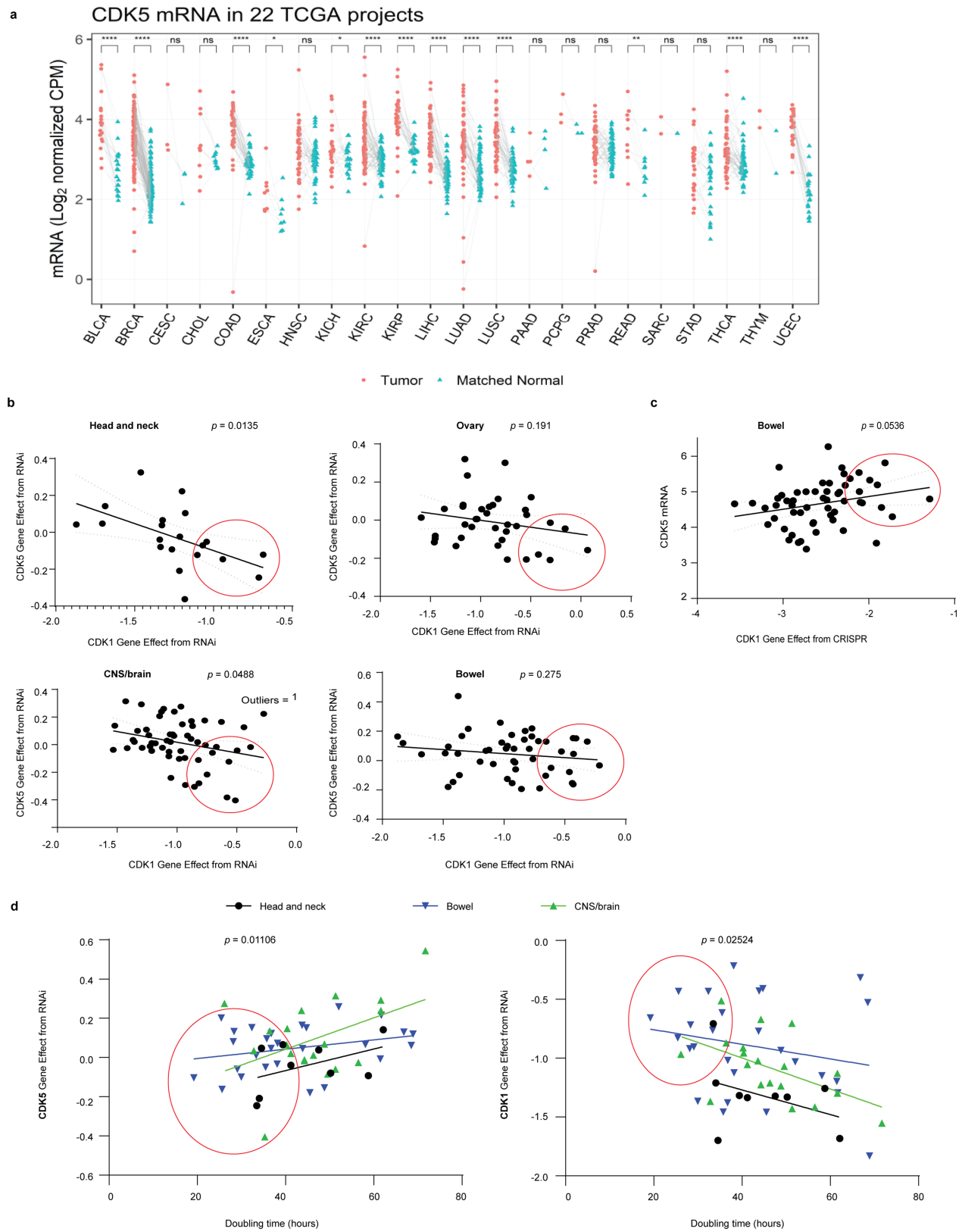


Extended Data Fig. 11 | RPE-1 harbouring CDK5-as introduced by CRISPR-mediated knock-in recapitulates chromosome mis-segregation defects observed in RPE-1 overexpressing CDK5-as upon inhibition of CDK5-as by 1NM-PP1 treatment. **a**, Chromatogram showing RPE-1 that harbours the homozygous CDK5-as mutation F80G introduced by CRISPR-mediated knock-in (lower panel), replacing endogenous WT CDK5 (upper panel).

b, Immunoblots showing level of CDK5 expressed in parental RPE-1 and RPE-1

that harbours CDK5-as F80G mutation in place of endogenous CDK5. **c**, Representative images of CDK5-as knocked-in RPE-1 cells exhibiting lagging chromosomes following indicated treatments. **d**, Quantification of percentage of cells exhibiting lagging chromosomes following indicated treatments shown in (c). Data represent mean \pm s.d. of three independent experiments from n = 252 DMSO, n = 220 1NM-PP1, where n is the number of cells. p-value was determined by two-tailed Mann Whitney U test.

Article



Extended Data Fig. 12 | See next page for caption.

Extended Data Fig. 12 | CDK5 is highly expressed in post-mitotic neurons and overexpressed in cancers. **a**, CDK5 RNAseq expression in tumours (left) with matched normal tissues (right). The data are analysed using 22 TCGA projects. Note that CDK5 expression is higher in many cancers compared to the matched normal tissues. BLCA, urothelial bladder carcinoma; BRCA, breast invasive carcinoma; CESC cervical squamous cell carcinoma and endocervical adenocarcinoma; CHOL, cholangiocarcinoma; COAD, colon adenocarcinoma; ESCA, esophageal carcinoma; HNSC, head and neck squamous cell carcinoma; KICH, kidney chromophobe; KIRC, kidney renal clear cell carcinoma; KIRP, kidney renal papillary cell carcinoma; LIHC, liver hepatocellular carcinoma; LUAD, lung adenocarcinoma; LUSC, lung squamous cell carcinoma; PAAD, pancreatic adenocarcinoma; PCPG, pheochromocytoma and paraganglioma; PRAD, prostate adenocarcinoma; READ, rectum adenocarcinoma; SARC, sarcoma; STAD, stomach adenocarcinoma; THCA, thyroid carcinoma; THYM, thymoma; and UCEC, uterine corpus endometrial carcinoma. *p*-value was determined by two-sided Student's t-test. ****: $p < 0.0001$; **: $p < 0.001$; **: $p < 0.01$; *: $p < 0.05$; ns: not significant, $p > 0.05$. **b**, Scatter plots showing cells of indicated cancer types that are more dependent on CDK5 and less dependent on CDK1. Each dot represents a cancer cell line. The RNAi dependency data (in DEMETER2) for CDK5 and CDK1 were obtained from the Dependency Map (depmap.org). The slope line represents a simple linear regression analysis for the indicated cancer type. The four indicated cancer types (Head/Neck, Ovary, CNS/Brain, and Bowel) showed a trend of more negative CDK5 RNAi effect scores (indicative of more dependency) with increasing CDK1RNAi effect scores (indicative of less dependency). The *p* value represents the significance of the correlation computed from a simple linear regression analysis of the data. Red circle highlights the subset of the cells that are relatively less dependent on CDK1 but more dependent on CDK5. **c**, Scatter plots showing bowel cancer cells

that expresses CDK5 while being less dependent on CDK1. Each dot represents a cancer cell line. The data on gene effect of CDK1 CRISPR and CDK5 mRNA level were obtained from the Dependency Map (depmap.org). The slope line represents a simple linear regression analysis. Red circle highlights the subset of cells that are relatively less dependent on CDK1 but expresses higher level of CDK5. For **b** and **c**, solid line represents the best-fit line from simple linear regression using GraphPad Prism. Dashed lines represent 95% confidence bands of the best-fit line. *p*-value is determined by the F test testing the null hypothesis that the slope is zero. **d**, Scatter plots showing rapidly dividing cells of indicated cancer types that are more dependent on CDK5 and less dependent on CDK1. Each dots represents a cancer cell line. The doubling time data on the x-axis were obtained from the Cell Model Passports (cellmodelpassports.sanger.ac.uk). The RNAi dependency data (in DEMETER2) for CDK5, or CDK1, on the y-axis were obtained from the Dependency Map (depmap.org). Only cell lines with doubling time of less than 72 h are displayed and included for analysis. Each slope line represents a simple linear regression analysis for each cancer type. The indicated three cancer types were analysed and displayed because they showed a trend of faster proliferation rate (lower doubling time) with more negative CDK5 RNAi effect (more dependency) but increasing CDK1 RNAi effect (less dependency) scores. The *p* value represents the significance of the association of the three cancer types combined, computed from a multiple linear regression analysis of the combined data, using cancer type as a covariate. Red circle depicts subset of fast dividing cells that are relatively more dependent on CDK5 (left) and less dependent on CDK1 (right). Solid lines represent the best-fit lines from individual simple linear regressions using GraphPad Prism. *p*-value is for the test with the null hypothesis that the effect of the doubling time is zero from the multiple linear regression RNAi - Intercept + Doubling Time (hours) + Lineage.

Reporting Summary

Nature Portfolio wishes to improve the reproducibility of the work that we publish. This form provides structure for consistency and transparency in reporting. For further information on Nature Portfolio policies, see our [Editorial Policies](#) and the [Editorial Policy Checklist](#).

Statistics

For all statistical analyses, confirm that the following items are present in the figure legend, table legend, main text, or Methods section.

n/a Confirmed

- The exact sample size (n) for each experimental group/condition, given as a discrete number and unit of measurement
- A statement on whether measurements were taken from distinct samples or whether the same sample was measured repeatedly
- The statistical test(s) used AND whether they are one- or two-sided
Only common tests should be described solely by name; describe more complex techniques in the Methods section.
- A description of all covariates tested
- A description of any assumptions or corrections, such as tests of normality and adjustment for multiple comparisons
- A full description of the statistical parameters including central tendency (e.g. means) or other basic estimates (e.g. regression coefficient) AND variation (e.g. standard deviation) or associated estimates of uncertainty (e.g. confidence intervals)
- For null hypothesis testing, the test statistic (e.g. F , t , r) with confidence intervals, effect sizes, degrees of freedom and P value noted
Give P values as exact values whenever suitable.
- For Bayesian analysis, information on the choice of priors and Markov chain Monte Carlo settings
- For hierarchical and complex designs, identification of the appropriate level for tests and full reporting of outcomes
- Estimates of effect sizes (e.g. Cohen's d , Pearson's r), indicating how they were calculated

Our web collection on [statistics for biologists](#) contains articles on many of the points above.

Software and code

Policy information about [availability of computer code](#)

Data collection

Cell counting for proliferation assay was performed using CountessTM 3 Automated Cell Counter (Invitrogen, AMQAX2000).

Immunofluorescence microscopy imaging was performed on a spinning disk confocal microscope (a Nikon Ti2 with a Yokogawa CSU-W1 spinning disk head). Z-stack images at 0.5- μm spacing were collected with a 60x/1.40 NA Plan Apochromat oil immersion objective (Nikon).

High resolution live cell imaging was performed on a Nikon Ti2 inverted microscope fitted with a Yokogawa CSU-W1 spinning disk head. Z-stacks (+6 (above) and -4 (below) at 0.75- μm spacing) were collected every 2 minutes for 2 hours, using a CoolSnap HQ2 CCD camera (Photometrics), and a 100x/1.45 NA Plan Apochromat Lambda oil immersion objective (Nikon). An environmental enclosure was used to maintain cell culture conditions (37°C and humidified 5% CO₂) for all live-cell confocal imaging.

Western blots were developed using Cytiva ImageQuantTM 800.

Nano-liquid chromatography-tandem mass spectrometry: Phosphopeptide-enriched samples were analyzed by LC-MS/MS on an Easy-nLC 1000 (Thermo Scientific) coupled to an Orbitrap™ Eclipse™ Tribrid™ mass spectrometer (Thermo Scientific) operated in positive ion mode with a FAIMS Pro™ Interface.

Data analysis

Fixed cell imaging analysis was performed using ImageJ/Fiji. Region of interest (ROI) was either manually drawn around cell boundaries (for 60x mitotic cells) or defined using image segmentation (for 20X primary nuclei). Li or Otsu thresholding was employed for nuclear segmentation on maximum intensity projections of Z-stacks of images acquired using 405nm laser (DAPI-stained). Images were converted into binary, the objects (nuclei) were processed using "Erode" and "Dilate" processing tools in ImageJ/Fiji. Lastly, the clumped nuclei was

separated using Watershed Separation program using Image J/Fiji. The ROIs generated were then overlaid on the 405nm images and used to measure circularity and solidity using Image J/Fiji shape descriptor tools. For measuring nuclear parameters, cells were imaged with a 20x objective in 8x8 tiles. The tiles were stitched and at least 200 cells were analyzed per image. Lobular, fragmented (including “bunch-of-grapes”) nuclei or nuclei containing blebs, folds and/or crevices were manually scored as abnormal nuclei. For quantification of fluorescence intensity of labeled proteins, ROIs were defined as described above and either total (mean * total area) or normalized intensity was determined in the indicated channel following background subtraction (determined from ROI outside the cell). Normalization was performed to total DAPI intensity. The Manders’ overlap coefficients were derived using the JACoP Fiji tool for colocalization analysis. The thresholding was kept constant throughout the images analyzed.

Shotgun mass spectrometry data analysis. Raw MS/MS spectra from the analysis were searched against reviewed Human Universal Protein Resource (UniProt) sequence database release 2021_06 with common laboratory contaminants using MaxQuant/Andromeda (PMID: 27809316) version 1.6.17.0. The search was performed with tryptic enzyme constraint set for up to two missed cleavages, oxidized methionine and phosphorylated serine, threonine and tyrosine set as a variable modification, and carbamidomethylated cysteine set as a static modification. Peptide MH⁺ mass tolerances were set at 20 ppm. The overall FDR was set at ≤0.25% using a reverse database target decoy approach. Phosphopeptide site localization was determined by MaxQuant and converted to phosphorylation sites and reverse hits and potential contaminants were excluded from further analysis using Perseus version 1.6.1.1 (PMID: 27348712). Phosphosite instances were uniquely identified by leading proteins, phosphorylation site, and multiplicity. The phosphosite instances with localization probability of less than or equal to 0.75 were filtered out. Phosphosite and protein intensity results were normalized by scaling each TMT channel to the channel median and then log2 transformed.

Quantitative proteomics data were further processed with LIMMA package (3.52.2) 53 via R version 4.1.3 54. Pairwise comparisons were performed among experimental conditions. A standard linear model fitting and an empirical Bayes procedure were performed to correct the distribution. A moderated t-statistic using a simple Bayesian model was applied as the fundamental statistic, followed by multiple test correction through the Benjamini-Hochberg method, which is referred to as false discovery rate (FDR). All these procedures are performed via limma with default configuration. The volcano plots were created using ggplot255 and ggrepel56 packages and used to visualize significantly different proteins and phosphosites. Gene Ontology enrichment analysis was performed with Cellular Component subontology using the clusterProfiler Bioconductor package version 4.6.257.

Analysis of mRNA Expression of TCGA tumors. For the analysis of RNASeq mRNA expression of the Cancer Genome Atlas (TCGA) tumor vs matched normal tissues, the raw HTSeq mRNA expression counts of all TCGA samples were downloaded from NCI Genomic Data Commons Data Portal (<https://portal.gdc.cancer.gov/>). The raw counts were normalized as counts per millions (CPMs) with TMM (weighted trimmed mean of M-values) and log2 transformed using the edgeR package. Tumor and matched normal tissues were identified with sample type code of 1, and 11, respectively. The ggpubr R package was used to perform the two-sided Student’s t-test to show the difference in CDK5 mRNA expression levels (log2-CPMs) between the tumor and the matched normal tissue groups for each cancer type. The test results and the log2-CPMs data were plotted using the ggplot2 version 3.5.1 package in R.

CDK5-cyclin B1 complex structure prediction. Amino acid sequences for human CDK5 (UniProt entry# Q00535), cyclin B1 (UniProt entry# P14635), and CDK1 (UniProt entry# P06493) were retrieved from UniProtKB. Structural models of heterodimer complexes between CDK5-cyclin B1 and CDK1-cyclin B1 were predicted using web-based ColabFold based on AlphaFold2- Multimer (AF2) code hosted by Google Colab (<https://colab.research.google.com/github/sokryton/ColabFold/blob/main/AlphaFold2.ipynb#scrollTo=G4yBrceuFbf3>)62. For each prediction, default parameters for the run including num recycles=3 and num models=5 were used, and the models were ranked based on interface-predicted template modelling (iPTM) score. Initially, for all proteins, full-length sequences were used as input for the prediction. Then the truncated cyclin B1 protein sequence was determined by analyzing the resulting complex structures to eliminate unnecessary regions that are neither part of the dimer interface nor contributing to any intramolecular interactions. Since most of the predicted models for each protein pair had excellent iPTM scores (0.9 or higher), all 5 models for each prediction were aligned and analyzed for any significant changes in the models. All structural analyses and figures were generated using Pymol (Schrödinger, Inc). Final models for CDK5-cyclin B1 and CDK1-cyclin B1 were generated by running top rank models (from AF2 predictions) through the Protein Preparation wizard in Schrödinger suite. All minimizations were performed with OPLS4 force field63.

Quantification of immunoblots intensity was performed using ImageJ.

Prism 10 (Graphpad Software Inc.) was used for indicated statistical analysis and production of all graphs and plots.

For manuscripts utilizing custom algorithms or software that are central to the research but not yet described in published literature, software must be made available to editors and reviewers. We strongly encourage code deposition in a community repository (e.g. GitHub). See the Nature Portfolio [guidelines for submitting code & software](#) for further information.

Data

Policy information about [availability of data](#)

All manuscripts must include a [data availability statement](#). This statement should provide the following information, where applicable:

- Accession codes, unique identifiers, or web links for publicly available datasets
- A description of any restrictions on data availability
- For clinical datasets or third party data, please ensure that the statement adheres to our [policy](#)

All data are available in the main paper or its Supplementary Information. The LC-MS/MS proteomics data have been deposited to the ProteomeXchange Consortium 58(<http://proteomecentral.proteomexchange.org>) via the PRIDE59 partner repository with the dataset identifier PXD038386 (username: reviewer_pxd03836@ebi.ac.uk; password:4st2Zrbp). Correspondence regarding experiments and requests for materials should be addressed to A.S. Spektor and D.C.

Research involving human participants, their data, or biological material

Policy information about studies with [human participants or human data](#). See also policy information about [sex, gender \(identity/presentation\), and sexual orientation](#) and [race, ethnicity and racism](#).

Reporting on sex and gender

N/A

Reporting on race, ethnicity, or other socially relevant groupings

N/A

Population characteristics

N/A

Recruitment

N/A

Ethics oversight

N/A

Note that full information on the approval of the study protocol must also be provided in the manuscript.

Field-specific reporting

Please select the one below that is the best fit for your research. If you are not sure, read the appropriate sections before making your selection.

Life sciences Behavioural & social sciences Ecological, evolutionary & environmental sciences

For a reference copy of the document with all sections, see nature.com/documents/nr-reporting-summary-flat.pdf

Life sciences study design

All studies must disclose on these points even when the disclosure is negative.

Sample size

All experiments were repeated independently at least two times that render reproducible results. Most experiments were repeated three to four times with reproducible results. In each imaging experiment, at least 25 cells per condition were imaged to select representative images. For quantification of phenotypes, 50 to 500 cells were used, as detailed in the figure legends.

Data exclusions

No data was excluded

Replication

All experiments were repeated independently at least two times that render reproducible results. Most experiments were repeated three to four times with reproducible results.

Randomization

Cells used for microscopy quantifications were randomly selected and analyzed with no sub-sampling.

Blinding

Investigator was blinded during live cell imaging data collection and subsequent analysis. Western blot, IP-WB, and gel image-related data generation were automated and therefore not subjected to blinding.

Reporting for specific materials, systems and methods

We require information from authors about some types of materials, experimental systems and methods used in many studies. Here, indicate whether each material, system or method listed is relevant to your study. If you are not sure if a list item applies to your research, read the appropriate section before selecting a response.

Materials & experimental systems

n/a	Involved in the study
<input type="checkbox"/>	<input checked="" type="checkbox"/> Antibodies
<input type="checkbox"/>	<input checked="" type="checkbox"/> Eukaryotic cell lines
<input checked="" type="checkbox"/>	<input type="checkbox"/> Palaeontology and archaeology
<input checked="" type="checkbox"/>	<input type="checkbox"/> Animals and other organisms
<input checked="" type="checkbox"/>	<input type="checkbox"/> Clinical data
<input checked="" type="checkbox"/>	<input type="checkbox"/> Dual use research of concern
<input checked="" type="checkbox"/>	<input type="checkbox"/> Plants

Methods

n/a	Involved in the study
<input checked="" type="checkbox"/>	<input type="checkbox"/> ChIP-seq
<input checked="" type="checkbox"/>	<input type="checkbox"/> Flow cytometry
<input checked="" type="checkbox"/>	<input type="checkbox"/> MRI-based neuroimaging

Antibodies

Antibodies used

The antibodies used in this study were as follows: mouse β -tubulin (B-7) Santa Cruz sc-5268 1:500 for IB, IF; mouse β -actin (C4) Santa

Antibodies used

Cruz sc-47778 1:500 for IB; rabbit CDK1 [EPR165] ab133327, 1:10,000 for IB, IF; mouse Cdc2 p34 (sc-54 AC) 25µL slurry used per mg of lysate for IP; mouse CDK2 (D-12) Santa Cruz sc-6248, 1: 500 for IB; rabbit CDK5 [EP715Y] Abcam ab40773 1:200 for IF; 1:1,000 for IB; mouseCDK5 (J-3) Santa Cruz sc-6247 1:500 for IB; mouse CDK5 (DC 17) Santa Cruz sc-249 AC, 25µL slurry used per mg of lysate for IP; human anti-centromere Centromere Antibodies Incorporated 15-235, 1:500 for IF; mouse c-Myc (9E10) Santa Cruz sc-40 1:500 for IB; rabbit c-Myc [Y69] Abcam ab32072, 1:100 for IF, 1:500 for IB, 2.5µg for IP; rabbit cyclin A2 Novus Biologicals NBP131330 1:500 for IB; rabbit cyclin B1 [Y106] Abcam ab32053, 1:200 for IF; rabbit cyclin B1 Abcam ab2949, 1:1,000 for IB; mouse cyclin B1 (GNS1) Santa Cruz sc-245 1:500 for IB; 1:400 for IF; mouse cyclin B1 (D-1) Santa Cruz sc-166210 AC, 25µL slurry used per mg of lysate for IP; mouse FLAG Sigma F1804 1:1,000 for IB; rabbit FLAG Bethyl A190-102A 1:1,000 for IB; rabbit HA-Tag (C29F4) Cell Signaling Technology 3724 1:500 for IB; rabbit KIF20A/RAB6KIFL Thermo Fisher Scientific 501730568 1:1,000 for IB; normal Rabbit IgG Cell Signaling Technology 27295 5µL used per IP; normal mouse IgG Santa Cruz SC-2025 5µL used per IP; mouse NuMA1 Life Technologies MA5-17293 1:500 for IB; IF; rabbit p35/25 (C64B10) Cell Signaling Technology 2680 1:500 for IB; mouse p35 (4G11) Santa Cruz sc-293184 1:1000 for IB; rabbit p39 EPR5074 Abcam ab124896 1:1000 for IB; rabbit phospho-CDK5 (Ser159) Life Technologies PA564751 1:500 for IB; rabbit phospho-Histone H3 Serine10 Cell Signaling Technology 9701, 1:500 for IB; phospho-Ser/Pro antibody; rabbit phospho (Ser)CDKs substrate P-S2-100 Cell Signaling Technology 9477S 10µL was used per IP; rabbit PP4R3/SMEK2 Abcam Ab224222, 1:50 for IF; PP4R3/SMEK2 rabbit phospho-S840 GL Biochem Ltd, custom made, 1:100 for IF; and mouse vinculin (H-10) Santa Cruz sc-25336, 1:1,000 for IB. IF: immunofluorescence; IB: immunoblotting; IP: immunoprecipitation.

Validation

All antibodies used in this study were acquired from commercial sources and validated for specificity and species reactivity by manufacturer.

Eukaryotic cell lines

Policy information about [cell lines and Sex and Gender in Research](#)

Cell line source(s)

293T, HeLa, and RPE-1 were obtained from ATCC. Modified cell lines (CRISPR knockout, over-expressing lines) were created in our lab.

Authentication

1. Parental 293T, HeLa and RPE-1 were validated by STR at ATCC.
2. Modified cell lines were confirmed by immunoblotting and/or genomic sequencing for the protein/gene of interest.

Mycoplasma contamination

All cell lines tested negative for mycoplasma using MycoAlert Plus Mycoplasma Detection Kit (Lonza).

Commonly misidentified lines
(See [ICLAC](#) register)

No commonly misidentified cell lines were used in this study.

Plants

Seed stocks

N/A

Novel plant genotypes

N/A

Authentication

N/A